Published in final edited form as:
Matrix Biol. 2023 August ; 121: 127–148. doi:10.1016/j.matbio.2023.06.004.

Absence of TRIC-B from type XIV Osteogenesis Imperfecta osteoblasts alters cell adhesion and mitochondrial function – A multi-omics study

Milena Jovanovic[a], **Apratim Mitra**[b], **Roberta Besio**[c], **Barbara Maria Contento**[c], **Ka Wai Wong**[d,e], **Alberta Derkyi**[f], **Michael To**[d,e], **Antonella Forlino**[c], **Ryan K Dale**[b], **Joan C Marini**[a]

[a]Section on Heritable Disorders of Bone and Extracellular Matrix, *Eunice Kennedy Shriver* National Institute of Child Health and Human Development, National Institutes of Health, Bethesda, United States.

[b]Bioinformatics and Scientific Programming Core, *Eunice Kennedy Shriver* National Institute of Child Health and Human Development, National Institutes of Health, Bethesda, United States.

[c]Department of Molecular Medicine, Biochemistry Unit, University of Pavia, Pavia, Italy.

[d]Department of Orthopaedics and Traumatology, The University of Hong KongShenzhen Hospital (HKU-SZH), Shenzhen, China.

[e]Department of Orthopaedics and Traumatology, Li Ka Shing Faculty of Medicine, The University of Hong Kong, Hong Kong, China.

[f]Office of the Clinical Director, *Eunice Kennedy Shriver* National Institute of Child Health and Human Development, National Institutes of Health, Bethesda, United States.

Abstract

Osteogenesis Imperfecta (OI) is a heritable collagen-related bone dysplasia characterized by bone fractures, growth deficiency and skeletal deformity. Type XIV OI is a recessive OI form caused by null mutations in *TMEM38B*, which encodes the ER membrane intracellular cation channel TRIC-B. Previously, we showed that absence of *TMEM38B* alters calcium flux in the ER of OI patient osteoblasts and fibroblasts, which further disrupts collagen synthesis and secretion. How the absence of *TMEM38B* affects osteoblast function is still poorly understood.

Communicating author and Reprint Requests: Joan C Marini, MD, PhD, Chief, Section on Heritable Disorders of Bone and Extracellular Matrix, NICHD, NIH, Bldg. 49; Rm 5A52, 49 Convent Drive, Bethesda, MD 20892, (cell) 301-792-6081, oidoc@helix.nih.gov.

Author contributions

Milena Jovanovic: Conceptualization, Investigation, Project administration, Validation, Visualization, Writing - original draft, Writing – review & editing. **Apratim Mitra**: Software, Writing – review & editing. **Roberta Besio**: Investigation, Writing – review & editing. **Barbara Maria Contento**: Investigation. **Ka Wai Wong**: Resources, Writing – review & editing. **Alberta Derkyi**: Investigation (clinical), Writing: review & editing. **Michael To**: Resources, Writing – review & editing. **Antonella Forlino**: Funding acquisition, Supervision, Writing – review & editing. **Ryan K Dale**: Software, Writing – review & editing. **Joan C Marini**: Conceptualization, Funding acquisition, Project administration, Supervision, Visualization, Writing - original draft, Writing – review & editing.

Declaration of Competing Interest
No conflict of interest for all authors.

Here we further investigated the role of *TMEM38B* in human osteoblast differentiation and mineralization. *TMEM38B*-null osteoblasts showed altered expression of osteoblast marker genes and decreased mineralization. RNA-Seq analysis revealed that cell-cell adhesion was one of the most downregulated pathways in *TMEM38B*-null osteoblasts, with further validation by real-time PCR and Western blot. Gap and tight junction proteins were also decreased by TRIC-B absence, both in patient osteoblasts and in calvarial osteoblasts of *Tmem38b*-null mice. Disrupted cell adhesion decreased mutant cell proliferation and cell cycle progression. An important novel finding was that *TMEM38B*-null osteoblasts had elongated mitochondria with altered fusion and fission markers, MFN2 and DRP1. In addition, *TMEM38B*-null osteoblasts exhibited a significant increase in superoxide production in mitochondria, further supporting mitochondrial dysfunction. Together these results emphasize the novel role of *TMEM38B*/TRIC-B in osteoblast differentiation, affecting cell-cell adhesion processes, gap and tight junction, proliferation, cell cycle, and mitochondrial function.

Keywords

Osteogenesis Imperfecta; TRIC-B; *TMEM38B* ; Cell adhesion; Mitochondrial fission/fusion; Osteoblast differentiation

Introduction

Osteogenesis Imperfecta (OI) or “brittle bone disease” is a rare, heterogeneous skeletal disorder with an incidence of 1/15–20,000 births. OI is clinically characterized by bone fragility, skeletal deformities, and growth deficiency, with secondary changes in other connective tissues such as dentinogenesis imperfecta, blue sclerae, hearing loss, cardiovascular and respiratory defects. Previously, OI was considered a dominant disorder caused by mutations in type I collagen genes, *COL1A1* and *COL1A2*, that encode α1(I) and α2(I) chains of collagen type I, respectively. These dominantly inherited OI types affect the structure or quantity of synthetized collagen. Although the majority of OI cases (~85%) are caused by dominant mutations in collagen genes, today OI is described as a collagen-related disorder with recessive forms caused by mutations in genes whose products interact with collagen and are critical for collagen folding, modification or processing, as well as osteoblast differentiation and mineralization (1,2).

Type XIV OI is a recessive OI form caused predominantly by null mutations in *TMEM38B*, which encodes the ER membrane trimeric intracellular cation channel type B (TRIC-B). TRIC-B is ubiquitously expressed in the ER and, together with the inositol 1,4,5-trisphosphate receptor (IP3R), affects Ca^{2+} flux from the ER to cytoplasm (3). Ca^{2+} signaling is crucial for collagen metabolism and post-translational modification (4). ER-Ca^{2+} flux kinetics were shown to be impaired in human *TMEM38B*-null osteoblasts and fibroblasts. Imbalance in ER-Ca^{2+} signaling induces ER stress and affects collagen synthesis and secretion resulting in abnormal collagen assembly and posttranslational modifications (4). In particular, the hydroxylation of type I collagen helical lysines by LH1 is reduced in *TMEM38B*-null cells (4), presumptively through the dependence of LH1 on the PPIase function of CyPB, an ER-resident cyclophilin which is in turn dependent on calreticulin/calmodulin interactions, as demonstrated for other chaperons (5,6).

The first reports of a mutation in *TMEM38B* described Bedouin families from Israel and Saudi Arabia, with a homozygous deletion of exon 4 (7,8). Subsequently, homozygous deletion mutation of exons 1 and 2 (9), as well as a homozygous nonsense variant in exon 4 of the *TMEM38B* gene were identified as causative mutations of type XIV OI (10). These mutations are all presumptively null, although *TMEM38B* Western blots were not included in the mutation reports. The only reported mutation that is not clearly predictive of a null outcome is a homozygous acceptor splice site variant in intron 3 (10), which was demonstrated to result in the insertion of 6 bp between exons 3 and 4 in *TMEM38B* cDNA. This could cause insertion of two amino acids in the TRIC-B TM2 region, which is involved in channel gating, and impair channel function. Western blots for stability of TRIC-B with a small insertion and functional studies of calcium flux were not reported. The absence of TRIC-B was demonstrated by Western blot (4) in patients with the Bedouin founder mutation, a stop codon and a compound heterozygote for the Albanian deletion and a small duplication.

The clinical phenotype of type XIV OI varies substantially, ranging from asymptomatic to severe. The most common clinical features include bone fractures, bowed limbs, osteoporosis, with tendency of fracture frequency improvement after puberty. The bone phenotype of type XIV OI is atypical compared to other OI subtypes that are usually characterized by high bone turnover and bone hypermineralization. Histomorphometry analysis showed type XIV OI bone has low trabecular bone volume and low bone turnover in combination with low osteoblast and osteoclast number, and, in most cases, bone matrix mineralization is normal on bone mineral density distribution (BMDD) (11).

The underlying molecular mechanism by which *TMEM38B* affects osteoblast function is poorly understood. Here, we describe the novel role of *TMEM38B* in regulation of osteoblast differentiation and mineralization. Our results show that cellular adhesion processes, proliferation, and cell cycle, as well as mitochondrial fission/fusion processes, are dysregulated in type XIV OI osteoblasts.

Results

Osteoblasts with *TMEM38B*-null mutation have altered differentiation and decreased mineral deposition *in vitro*

TMEM38B-null osteoblasts were derived from surgical bone chip discard from a 13-year-old male patient. He was previously reported to be compound heterozygous for the deletion encompassing *TMEM38B* exons 1 and 2 (first reported in 2014 in an Albanian child (9) and a novel c.63dupT, which directly introduces a premature termination codon in exon 1 (p.D22X) (4). The patient has a moderately severe OI phenotype (11). He was born to unrelated American parents of British/Scottish and British/German ancestry by spontaneous vaginal delivery as the 7 pounds, 9 ounces product of an uncomplicated term pregnancy. A femur fracture was noted at birth. His long bones are thin on radiographs, and he sustained 10 femur fractures and 7 tibial fractures; his long bone deformities required multiple intramedullary rodding procedures. He has had progressively deforming scoliosis (currently 40° Cobb angle) and was noted to have moderate lower airway obstruction at age 22 years. His lumbar spine bone mineral density (BMD) z scores by dual-energy X-ray absorptiometry (DXA) were in the −4 to −5 range prior to receiving 3 years of pamidronate infusions, which elevated his z-score to the −2 to −3 range. He was noted at age 21 years to have tricuspid valve regurgitation. Hypertrophic cardiomyopathy and aortic root dilatation were noted at age 27, and increasing septal thickness was noted at age 34 years. He has relative macrocephaly (head circumference =58 cm, 98th percentile for male adults), Wormian bones around the lambdoidal suture, and a normal brain computerized tomography (CT) scan without basilar invagination. Facial appearance and dentition are normal. There is bilateral moderate conductive/mixed hearing loss amenable to amplification. He has short stature, with height at age 34 years comparable to a skeletally normal 15-year-old boy. He ambulates with a walker.

To investigate the role of *TMEM38B* in regulation of osteoblast differentiation and mineralization, we differentiated patient and control osteoblasts *in vitro* into mature osteoblasts. Cell lysates were collected at Day 0, 7, 14, and 21 of differentiation. Expression level of the early marker gene *COL1A1* was significantly reduced, while *ALPL* was significantly increased throughout differentiation. Mid- and late differentiation marker gene *IBSP* was significantly increased during early and late differentiation, *SPP1* was significantly increased throughout differentiation, whereas *SPARC* was significantly reduced in differentiated patient osteoblasts compared to control (Figure 1A). The osteoblast marker genes for late differentiation had opposing expression trends, with *DMP1* trending increased at Day 14, whereas *SOST* expression was reduced mid-differentiation in patient osteoblasts versus control (Figure 1A). These results confirmed our prior studies (11).

Expression of osteoblast genes that impact osteoclast development (Figure 1B) was altered in *TMEM38B*-null versus control osteoblasts. Expression of *RANKL*, an activator of osteoclast differentiation, was significantly decreased in mid to late differentiation, while *OPG*, which inhibits the stimulatory effect of *RANKL* on osteoclastogenesis, was close to control values except on Day 0. As a result, the *RANKL*/*OPG* ratio was significantly reduced throughout differentiation in *TMEM38B*-null osteoblasts versus control, indicating reduced stimulation of osteoclast development in the absence of *TMEM38B*.

We also investigated the mineralization capacity of patient versus control osteoblasts. For this study, patient and control osteoblasts were cultured in differentiation medium for 6 weeks, after which cell cultures were stained with Alizarin Red. Quantification of the stain confirmed a significant decrease of mineral deposition in *TMEM38B*-null osteoblast cultures compared to control (Figure 1C-D). Thus, the absence of *TMEM38B* expression in osteoblasts causes dysregulation of osteoblasts differentiation and mineralization.

RNA-Seq reveals downregulation of cell adhesion pathway in differentiated *TMEM38B*-null osteoblasts

To extend our understanding of the role of *TMEM38B* in osteoblast differentiation, we performed a bulk RNA sequencing analysis of patient and control osteoblasts at Day 0 and at weekly timepoints during 3 weeks of differentiation. Functional enrichment analysis indicated that cell adhesion processes, such as cell-cell adhesion and cell-junction, were among the most downregulated pathways in patient osteoblasts at Day 0 and at all 3 differentiation timepoints (Figure 2A-D). Although synapse assembly was also a highly affected pathway, osteoblasts do not share synapse function and many of these genes overlapped with the cell adhesion pathway.

Other pathways highly relevant for the role of *TMEM38B*-null osteoblasts in the bone dysplasia of OI are those governing the extracellular matrix (ECM) organization and/or extracellular structure organization. These pathways were significantly downregulated at Day 7, 14 and 21 compared to control osteoblasts (Figure 2B-D), and both shared the same genes, the changes in expression of which are presented as a heatmap in Supplemental Figure 1A.

On other hand, RNA-Seq analysis at Day 0 showed that the ECM organization and extracellular structure organization were the most upregulated pathways, as well as cartilage development and ossification (Supplemental Figure 2A). At Day 21 the cell-cell adhesion pathway was among the significantly upregulated pathways (Supplemental Figure 2B), however, most of the upregulated genes at that timepoint were not directly related to cell adhesion processes in bone but to other systems such as the nervous system (12–14).

Interestingly, the Notch signaling pathway was also upregulated in patient osteoblasts compared to control (Supplemental Figure 2B). Based on these results, we decided to focus our next steps on investigating the novel role of *TMEM38B* in cell adhesion during osteoblast differentiation.

RT-qPCR validation confirms transcript-level dysregulation of cell adhesion pathways in *TMEM38B*-null osteoblasts

Cell–cell and cell–matrix interactions are mediated by cell adhesion molecules (CAMs) including cadherins, integrins, selectins and immunoglobulin-like CAMs. CAMs have a role in regulation of various cell processes in addition to adhesion *per se*, such as proliferation, differentiation, apoptosis (15). We investigated whether absence of TRIC-B protein in cells of patient with type XIV OI, as had been previous demonstrated by Western blot (4), affects osteoblast adhesion processes. We assembled a set of significantly downregulated genes from the cell-cell adhesion pathway (Figure 2E, Supplemental Figure 3A-D) and further validated their mRNA expression levels by RT-qPCR.

Differentially expressed genes (DEGs), including clustered protocadherins and adhesion genes with a role in bone were validated. Clustered protocadherins from α, β and γ families were found to be downregulated in *TMEM38B*-null osteoblasts, with decreased mRNA expression levels throughout differentiation in patient versus control osteoblasts (Figure 2F). Protocadherins from the γ family (*PCDHGA7*, *PCDHGA12*) and β (*PCDHB10* & *PCDHB13)* showed strong expression levels (70–80th percentile) in control cells and were suppressed several-fold in *TMEM38B*-null cells. While other protocadherins (α (*PCDHA10*), β (*PCDHB7*, *PCDHB10*, *PCDHB11*, *PCDHB12*, *PCDHB13* and *PCDHB15*)), had moderate levels of expression (~50th percentile) in control and patient osteoblasts, the consistency of downregulation of the interrelated set was striking. Seven additional genes encoding proteins with a role in adhesion (*DCHS1*, *CLDN1*, *CADM1*, *ICAM1*, CELSR2, *PTPRF*, *PTPRD*) and known to function in bone were significantly downregulated in patient versus control osteoblasts throughout differentiation (Figure 2G).

Given the validation of adhesion molecules from the heatmap, we extended our investigation to cadherins. Cadherin-2/N-cadherin (*CDH2*) had significantly reduced mRNA expression levels in mid-differentiation (Day 7 and 21) in patient osteoblasts compared to control osteoblasts. On the other hand, Cadherin-4/R-cadherin (*CDH4*), remained significantly elevated in mid-differentiation (Day 7 and 14) in patient osteoblasts compared to control (Figure 2H). In addition, *CDH4* was also shown to be significantly elevated during differentiation in patient osteoblasts in comparison to another osteoblast control from 5-year-old male (Supplemental Figure 4A). Collectively these transcriptional results validate the finding that cell adhesion processes are disrupted, preponderantly by transcriptional downregulation, in *TMEM38B*-null osteoblasts. Unfortunately, patient osteoblasts sample were insufficient to correlate transcriptional downregulation of cell-adhesion genes with protein levels by Western blots.

Gap and tight junctions are reduced in *TMEM38B*-null osteoblasts

Gap and tight junctions are important structures for cell-cell communication, ensuring the proper signal transduction between cells, and both interact with cadherins, important molecules for cell adhesion (16,17). Gap junction formation and function would be impacted by decreased protein levels of gap and tight junction components. We analyzed the mRNA and protein levels of *GJA1*/Cx43 and *TJP1*/ZO-1 in patient *TMEM38B*-null osteoblasts and control. Expression of gap junction gene *GJA1*, encoding Cx43, was significantly reduced in mid-differentiation, while expression of tight junction gene *TJP1*, which encodes ZO-1, was significantly downregulated in early and mid-differentiation of type XIV OI patient osteoblasts versus control (Figure 3A). In addition, *TJP1* transcripts were shown to be downregulated in patient osteoblasts compared to another osteoblast control from a 5-year-old male (Supplemental Figure 4B). Cx43 protein was downregulated throughout differentiation in patient versus control osteoblasts, paralleling the timing of *GJA1*/Cx43 transcript levels during osteoblast differentiation. ZO-1 was also downregulated in patient osteoblasts at early stages of differentiation (Figure 3B-C). Immunocytochemistry staining of patient and control osteoblasts (Day 0) showed reduction in both Cx43 and ZO-1 signal in *TMEM38B*-null osteoblasts (Figure 3D-E).

Furthermore, we showed that gap and tight junctions are also altered in calvarial osteoblasts from an osteoblast-specific conditional knock-out murine model of *Tmem38b* (*Runx2Cre;Tmem38b*$^{fl/fl}$, cKO, (18)) compared to wildtype osteoblasts. Expression levels of *Gja1*/Cx43 and *Tjp1*/ZO-1 were significantly decreased throughout differentiation in murine cKO osteoblasts (Figure 3F). Immunocytochemistry staining of Cx43 and ZO-1 (Figure 3G-J) was significantly reduced in murine cKO osteoblasts compared to control, further supporting finding that deletion of the TRIC-B channel disturbs gap and tight junctions in osteoblasts.

Antibody array-based protein analyses reveal that cell adhesion and extracellular matrix organization are disrupted in *TMEM38B*-null osteoblasts

To explore which proteins are involved in type XIV OI pathophysiology, patient and control osteoblasts at Day 0 and differentiated osteoblasts at Day 14 were subjected to antibody array-based proteomics studies (RayBiotech Life, Inc.; Label-Based (L-Series) Human Antibody Array L-6000 Glass Slide Kit). Upregulated and downregulated proteins with fold change > 2 were further considered.

The most affected protein functions were related to protein refolding, secretion, response to reactive oxygen species (ROS), cell adhesion, ECM organization, Wnt, ossification, inflammatory response, and acute-phase response (Figure 4A). Secretion and ossification were predominantly reduced, especially at Day 0, in *TMEM38B*-null osteoblasts compared to control. Inflammatory and acute-phase response were highly affected at Day 14, shown by increased expression of representative proteins. Cell adhesion pathway components were both increased and reduced at Day 0, while proteins affected at Day 14 were mostly decreased. On the other hand, response to ROS included proteins that were strongly up- or downregulated at Day 14, with Day 0 mostly being reduced. Canonical Wnt signaling was increased at Day 0, then reduced at Day 14. ECM organization proteins were both increased and reduced at both timepoints. Protein refolding components were upregulated at Day 0, and then mostly downregulated at Day 14. The complete list of upregulated and downregulated proteins with > 2 fold change were shown in Supplemental Figure 5A.

The demonstration by antibody array-based proteomic analysis that cell adhesion is affected in *TMEM38B*-null osteoblasts complements and confirms the transcriptomics data. We validated several of the top protein hits using Western blot. PTK7 (protein tyrosine kinase 7), which functions in cell adhesion (19), was significantly increased at Day 0, and then significantly decreased at Day 14 in patient osteoblasts. PXN (paxillin), a molecule involved in focal adhesion (20), was also significantly increased at Day 0, and then subsequently decreased significantly at Day 14 by Western blot. On the antibody array, Day 0 PXN was not significantly altered, but showed a significant decrease on Day 14 in agreement with Western blot data. We considered Western blot results for PXN at Day 0 more robust, given the greater sensitivity of this technique compared to antibody array-based protein analysis. JAG1, a Notch ligand that regulates bone remodeling (21), was significantly increased at both Day 0 and Day 14 (Figure 4B-C). *HEY2*, one of the common downstream targets of Notch signaling, was significantly increased at early and late differentiation in patient osteoblasts compared to control (Supplemental Figure 6A).

Proliferation and cell cycle are disrupted in differentiated *TMEM38B*-null osteoblasts

Disrupted cell adhesion could also influence proliferation and cell cycle progression, Cell adhesion is a calcium-dependent process (22), and intracellular calcium is crucial for cell cycle progression and plays a vital role in the regulation of cell proliferation (23). To examine if absence of *TMEM38B* affects osteoblast proliferation, patient and control osteoblasts were labelled with BrdU for 24 hours and absorbance at 450 nm was read as a measure of proliferation. The BrdU proliferation assay showed approximately 20% decrease in proliferation in patient compared to control osteoblasts (Figure 5A). Consistent with the

BrdU assay, immunocytochemistry of Ki67 proliferation marker was significantly reduced in patient osteoblasts compared to control (Figure 5B-C). Transcript levels of several cell cycle markers were altered in *TMEM38B*-null osteoblasts. *CCND2*/Cyclin D2, and *CCNE1*/Cyclin E1 showed significantly reduced expression throughout differentiation timepoints in patient osteoblasts versus control. Conversely, expression of *CCNE2*/Cyclin E2, *CCNB1*/Cyclin B1, and *CCNB2*/Cyclin B2 were significantly upregulated in patient osteoblasts versus control (Figure 5E). However, on Western blots, all cyclins tested (Cyclins D1, D2, D3, and B1) were significantly downregulated in patient osteoblasts compared to control (Figure 5F-G).

Another factor with the potential to contribute to decreased proliferation as well as to disrupt cell adhesion in *TMEM38B*-null osteoblasts is connective tissue growth factor (CTGF), encoded by *CCN2.* CTGF has a role in proliferation, differentiation, migration, and cell adhesion. RNA-Seq data analysis showed that at Day 7, *CCN2*/CTGF is one of the genes included in downregulated extracellular structure organization (Figure 5H). When validating downregulation of *CCN2*/CTGF transcripts in *TMEM38B*-null osteoblasts by RT-qPCR, we found that *CCN2*/CTGF expression was significantly reduced throughout differentiation in patient osteoblasts versus control (Figure 5I). Western blots showed a significant reduction of CTGF in differentiated patient osteoblasts (Figure 5J, Supplemental Figure 7A). These results demonstrate that *TMEM38B* deletion decreases proliferation and cell cycle progression, and that this may be directly related to dysregulated cell adhesion, further affecting osteoblast differentiation.

Increased ER stress associated with mitochondrial fission/fusion abnormalities in *TMEM38B*-null osteoblasts

TRIC-B channel deficiency was shown to affect ER calcium flux in osteoblasts (4), which further caused ER stress and underlies the disruption of collagen synthesis. One collagen chaperone, HSP47, is a marker of collagen ER retention due to misfolding of collagen (24). To investigate whether HSP47 is affected due to *TMEM38B*-related ER stress, we measured its transcript and protein levels. *SERPINH1*/HSP47 expression was significantly reduced at Days 0, 7 and 21 in patient osteoblasts compared to control (Figure 6A). Western blot showed an increase in HSP47 protein level on Day 0 osteoblasts, but a significant reduction throughout differentiation of patient osteoblasts versus control (Figure 6B-C). Immunocytochemistry of undifferentiated osteoblasts showed increased HSP47 in patient osteoblasts versus control, corroborating the Western blot Day 0 data (Figure 6D). These results suggest that even though HSP47 is moderately increased at basal level in *TMEM38B*-null osteoblasts due to ER-stress, during differentiation it fails to cope with the disrupted collagen synthesis. Electron microscopy of patient *TMEM38B*-null osteoblasts showed the expected ER dilatation in patient cells (Figure 7A).

Surprisingly, electron microscopy also revealed that mitochondria in patient osteoblasts had strikingly abnormal morphology, with a very elongated shape and evident cristolysis (Figure 7A). Contact sites between ER and mitochondria (ER-MCSs) have been shown to be the locations at which mitochondrial fusion and fission machineries localize and regulate mitochondrial morphology (25). The protein levels of markers for mitochondrial fission and fusion, DRP1 and MFN2 respectively, were significantly upregulated in patient osteoblasts early in differentiation, then lower in late differentiation points (Figure 7B-C).

In addition, we evaluated the production of ROS, specifically superoxide in mitochondria, in control and patient osteoblasts. Immunofluorescence staining of superoxide with MitoSox, a superoxide-specific dye, was highly increased in patient cells compared to control. Treating cells with MitoTEMPO, a mitochondrial antioxidant and a scavenger of superoxide for 24 hours, normalized the level of superoxide in *TMEM38B*-null osteoblasts to control level (Figure 7D). Also, mitochondrial ROS (mt-ROS) were significantly higher in *TMEM38B*-null osteoblasts, as measured by fluorescence intensity (Figure 7E). Alteration in mitochondrial function is a newly emerging finding for OI osteoblasts, which could further be explored in cell energetics study of *TMEM38B*-null osteoblasts, as there could be a potentially direct effect of prolonged ER stress on mitochondrial fusion or fission and mt-ROS production in *TMEM38B*-null osteoblasts.

Discussion

Recessive mutations in *TMEM38B*, resulting in absence of the intracellular TRIC-B cation channel, cause type XIV OI. TRIC-B impacts calcium flux kinetics in osteoblasts and fibroblasts, critical to multiple steps of collagen synthesis and secretion (4). Using osteoblasts from a patient with type XIV OI (4,11), we report here novel findings about additional roles of TRIC-B in osteoblast function, and the consequences of their disruption in OI (Figure 8). We took a multi-omics approach comprised of transcriptomics and antibody array-based proteomics, to show that absence of TRIC-B disrupts cell adhesion processes in patient osteoblasts. *TMEM38B*-null osteoblasts have reduced gap and tight junctions, together with decreased proliferation and impaired cell cycle progression. In addition, we show the first evidence that recessive OI patient osteoblasts exhibit changes in mitochondrial morphology, due to impaired fission/fusion processes, as well as increased mt-ROS production. Further, the Notch signaling pathway, important to bone remodeling, was altered in *TMEM38B*-null osteoblasts.

Disrupted cell-cell adhesion processes in *TMEM38B*-null osteoblasts

RNA-Seq transcriptomic data obtained from *TMEM38B*-null osteoblasts showed that cell-cell adhesion was among the most downregulated signaling pathways (Figure 2A-D). Cell adhesion is a dynamic process important for tissue assembly and cell-cell interactions (15). These connections or adherens junctions consist of multiprotein complexes including transmembrane cell adhesion molecules (cadherins), and peripheral membrane proteins (catenins) (15), which are important for initiation and stabilization of cell-cell adhesion, regulation of the actin cytoskeleton, intracellular signaling and transcriptional regulation (26). The calcium-dependent adhesive interactions of cadherins (22) are critical for stable tissue organization and function (27), as well as for regulation of cell proliferation, differentiation, and survival (15). Osteoblasts express a limited number of cadherins including cadherin-2 (N-cadherin), cadherin-4, and cadherin-11. Cadherin-2, important for osteoblast differentiation and N-cadherin mediated cell adhesion (28,29), had significantly reduced expression in *TMEM38B*-null osteoblasts (Figure 2H), while cadherin-4 expression was upregulated in *TMEM38B*-null osteoblasts. Differential timing of cadherin-2 and cadherin-4 expression has also been noted in visual systems (30), suggesting functionally different roles. These impaired cell-cell adhesion processes may contribute to altered *TMEM38B*-null osteoblast differentiation and reduced mineral deposition (Figure 1A, 1C-D).

Several validated genes from RNA-Seq downregulated cell-cell adhesion pathways have a role in development of craniofacial abnormalities, such as *DCHS1*, *PTPRF*, and *PTPRD*. Loss-of-function mutations in *DCHS1* (protocadherin-16) and *FAT4*, which act as a receptor-ligand pair, were shown to induce Van Maldergem syndrome, which includes craniofacial abnormalities such as maxillary hypoplasia, microtia and atresia of the external auditory meatus, as well as mitral valve prolapse. (31). In double *Dchs1*/*Fat4* knockout murine mutants, proliferation of osteoprogenitors is increased and osteoblast differentiation is delayed, identifying Dchs1-Fat4 as impacting osteoblast differentiation (32). Deletion of *PTPRF* and *PTPRD*, leukocyte antigen related (LAR) family receptor protein tyrosine phosphatases, also induced craniofacial abnormalities similar to Pierre-Robin sequence in a murine model, identifying them as contributors to craniofacial morphogenesis (33). PTPRF was also shown to be localized at and implicated in regulation of focal adhesions (34).

Facial dysmorphism has not been described in either our patient or other type XIV OI patients. Our patient has relative macrocephaly (58 cm, 98th centile) with normal brain magnetic resonance imaging, facial appearance, and dentition (11); he also has Wormian bone around the lambdoid suture. Other type XIV patients have been reported to have Wormian bones and relative macrocephaly. However, decreased expression of genes involved in cell adhesion that have a known effect on the skeleton would contribute to a more global downturn of cell adhesion genes in type XIV osteoblasts.

The products of other validated genes from RNA-Seq were directly involved in adhesion. *CADM1* or cell adhesion molecule-1 is expressed by osteoblasts and serves as a diagnostic marker for osteosarcoma (35). *ICAM1*, or intercellular adhesion molecule-1, is localized at the osteoblast surface, and mediates cellular interactions by binding to its counter-receptors lymphocyte function-associated antigen-1 (LFA-1), localized at the surface of osteoclast precursors. ICAM1 blockade between osteoblasts and osteoclast precursors results in inhibition of osteoclast recruitment (36). Clustered protocadherins, known for their role in vertebrate nervous system development and cancer pathogenesis (37), emerged as reasonable candidates for a signaling pathway in osteoblasts; further validation, including gene knockout, would be required to prove their function. *CLDN1* or Claudin 1 is one of the tight junction proteins; it has a positive role in osteoblast proliferation and differentiation (38). *CELSR2*, or cadherin EGF LAG seven-pass G-type receptor 2, is a candidate susceptibility gene in idiopathic scoliosis (39).

Antibody array-based proteomics analysis confirmed the importance of cell-cell adhesion in *TMEM38B*-null cells. PTK7, a catalytically defective receptor protein tyrosine kinase with a role in cell adhesion, canonical and non-canonical Wnt pathway, cell polarity (19,40), as well as PXN, a focal adhesion protein (20), were among the top hits identified by antibody array-based proteomics and validated by Western blot. Both were increased in undifferentiated osteoblasts, but then reduced during osteoblast differentiation, indicating that differentiation might be a factor in their reduction. PXN and its tyrosine phosphorylation have been shown to have a role in regulating LPS-induced mitochondrial fission, mt-ROS generation and endothelial cell barrier dysfunction in human lung endothelial cells (41). Another interesting antibody array-based proteomics hit involved upregulation of JAG1, a Notch 1 receptor ligand. Notch receptor maintains its native inactive structure via calcium binding, while chelation of calcium leads to activation (42). Notch activation by JAG1 induces the clustering of STIM2, a protein responsible for sensing of calcium level in the ER, which subsequently enhances store-operated calcium entry (SOCE) (43). In our previous study (4), *TMEM38B*-null fibroblasts had deficient SOCE shown by the intracellular calcium stores being more rapidly depleted compared to control. Thus, a TRIC-B impact on the Notch signaling pathway, important for bone remodeling (21), is a reasonable expectation. In addition, it has been shown that transfection of NIH3T3 cells with a secreted form of the extracellular domain of Jag1 caused decreased cell-matrix adhesion, as well as changes in cadherin-mediated intercellular junctions and focal adhesions, suggesting that Jag/Notch may contribute to regulation of cell-cell and cell-matrix interactions (44). Activation of Notch signaling late in osteoblast differentiation, detected by RNA-Seq analysis (Supplemental Figure 2B), is supported by increased expression of downstream target *HEY2* by RT-qPCR (Supplemental Figure 6A). In bone, activation of Notch 1 receptor by JAG1 also inhibits bone resorption by induction of OPG (21,45), an inhibitor of RANKL, which correlates with our results (Figure 1B).

Cell adhesion defects in OI models

Potential defects in cell adhesion processes have been identified in murine OI models, although those analysis were not validated. RNA-Seq analysis of osteocyte-enriched cortical long bones from *CrtapKO* mice, a recessive OI type VII model caused by loss of the prolyl 3-hydroxylation complex (46), and oim/oim mice, another recessive OI model with a mutation preventing α2(I) chain incorporation (47), showed dysregulated pathways related to cell adhesion (48). Cell adhesion also emerged as dysregulated from a mass spectrometry proteomics study using human fibroblasts from dominant OI type II and III, carrying *COL1A1* or *COL1A2* mutations (49).

Gap and tight junction alterations in *TMEM38B*-null osteoblasts

Interactions between cells are mediated via the cell junctional complex consisting of adherens junctions, tight junctions, gap junctions and hemidesmosomes. Tight and gap junctions are important for signal transduction between cells. Tight junctions are formed in regions where membranes of two cells are tightly connected, regulating the passage of ions and molecules between cells, and maintaining cell polarity. The tight junction protein zonula occludens protein 1 (ZO-1) is a cytoplasmic actin binding protein (50). Part of cadherin-based cell adhesion, ZO-1 facilitates direct interactions of cadherin/catenin complex with actin-based cytoskeleton (16). In addition, localization of ZO-1 is modulated by extracellular calcium (51). Gap junctions regulate the passage of ions and molecules between the cytoplasm of two adjacent cells and are formed by connexins. Intracellular calcium regulates the permeability of gap junctions composed of Cx43 (52). Cx43 is the most abundant connexin in bone; deletion of Cx43 in mice causes osteoblast dysfunction, craniofacial abnormalities, and delayed ossification (53). ZO-1 interacts with Cx43 and may facilitate gap junction-mediated communication and induce changes in membrane localization of Cx43 in osteoblastic cells (54). Our study demonstrated significant reduction of Cx43 and ZO-1 protein in both patient *TMEM38B*-null osteoblasts and also in murine calvarial osteoblasts from conditional *Tmem38b* knockout mice (Figure 3). The common impact of absent TRIC-B across species and different *TMEM38B* mutations emphasizes the important TRIC-B role in cell-cell communication.

CTGF involvement in *TMEM38B*-related cell adhesion defect

CTGF downregulation in *TMEM38B*-null osteoblasts is another likely contributor to their disrupted adhesion and differentiation. CTGF is a secreted, matricellular protein that has many cellular roles such as proliferation, differentiation, adhesion, and synthesis of ECM proteins. Specifically, CTGF enhances proliferation and differentiation of cultured osteoblasts (55). Furthermore, in the MC3T3-E1 pre-osteoblastic cell line, CTGF serves as an adhesive substrate for osteoblasts, via $\alpha_v\beta_1$ integrin, as well as cytoskeletal reorganization and osteoblast differentiation (56). CTGF-null mice had multiple skeletal dysmorphisms among other skeletal abnormalities, enlarged vertebrae, shortened sternum and mandibles, kinked ribs and long bones. (57).

Alterations of mitochondria function in *TMEM38B*-null osteoblasts

Finally, one of the major findings in this paper is the involvement of osteoblast mitochondria in type XIV OI pathological processes. We observed differences in mitochondrial morphology, consisting of striking elongation with crystolysis, along with altered expression of mitochondrial fission/fusion markers (DRP1, MFN2) and increased production of superoxide. The contact sites between ER and mitochondria (ER-MCSs) regulate many features of mitochondrial physiology and dynamics, such as mitochondrial fusion/fission, calcium, and lipid trafficking (58). Mitochondrial fission is regulated by the main dynamin-related GTPase DRP1, while fusion is driven by Mitofusin paralogs (MFN1 and MFN2). Fission and fusion processes are spatially coordinated and co-localized at ER-MCSs. Both mitofusins and DRP1 accumulate at ER-MCSs forming hotspots for membrane dynamics that can respond rapidly to metabolic signals (25). In addition, ER-MCSs are enriched with IP3Rs, thus play a central role in regulation of mitochondrial calcium level. Mitochondrial calcium levels are important for mitochondrial oxidative phosphorylation (OXPHOS), generation of ROS, and apoptosis (58). Levels of ROS H_2O_2 produced by mitochondria are induced by, and in turn influence, calcium signaling at ER-MCSs (59). ER-influenced mitochondrial dysfunction in *TMEM38B*-null osteoblasts may be induced by ER accumulation of misfolded collagen, with ER stress modified by the mitochondrial response. For example, osteoblasts from *COL1A2* G610C OI mice with dominant type IV OI undergo integrated stress response (ISR) due to ER accumulation of misfolded collagen. ISR is regulated by changes in expression of mitochondrial *Hspa9*/HSP70 (mt-HSP70) and ATF5; activation of *Hspa9* was speculated to be induced by disruption of mitochondria-associated ER membrane (60). However, mitochondrial dysfunction was previously observed in muscle tissue in OI murine models, where accumulation of misfolded type I collagen would not be expected. In gastrocnemius muscle of oim/oim mice, reduction of mitochondrial respiration rates, changes in mitochondrial biogenesis markers, mitophagy and electron transport chain components, were reported (61). *Mss51*, a metabolic stress inducible factor found in mitochondria, was downregulated in RNA-Seq analysis of oim/oim and Jrt murine gastrocnemius muscle (62). Much remains to learn about the role of mitochondria in OI.

Interestingly, data from triple-negative breast cancer cells (TNBC) has shown connections between mitochondrial metabolism and cell adhesion. Uncoupling of OXPHOS, an important mitochondrial metabolic pathway in various cancers, with FR58P1a induced mitochondrial dysfunction in TNBC that impaired fibronectin-dependent cell adhesion by decreasing β1-integrin at the cell surface (63). The cancer cell data raises the intriguing possibility that mitochondrial dysfunction and altered cell adhesion in *TMEM38B*-null osteoblasts may be interrelated.

Final remarks and future exploration

Our data revealed novel interconnected roles of *TMEM38B* in osteoblast differentiation and mineralization. Deletion of the TRIC-B channel, which affects ER-calcium flux kinetics, has myriad effects because of the importance of calcium to a broad range of skeletal processes. We demonstrated that human *TMEM38B*-null osteoblasts have a series of altered calcium-dependent cellular processes, such as disrupted cell adhesion in combination with decreased gap and tight junctions, cell proliferation, cell cycle progression, as well as alterations in mitochondria morphology and function.

Antibody array-based protein analyses revealed several affected pathways for type XIV OI osteoblasts. Altered protein refolding and reduced secretion contribute to cellular stress. Increased inflammatory response and acute-phase response might affect cellular components of bone and impact bone turnover. Alterations in ECM organization and cell adhesion could be expected to negatively affect cell-matrix cross talk, impairing osteoblast differentiation in general as well as osteoblast cytoskeletal structure in particular. Altered cytoskeletal structure in OI osteoblasts has been associated with altered cell proliferation and impaired secretion of both collagenous and non-collagenous matrix proteins (64). We speculate that, at the whole bone level, changes in osteoblast adhesion and cell-matrix interactions could negatively impact bone mechano-sensing and contribute to low bone mass and weaker bone geometry. Increased ROS might impair cell energetics and alter osteoblast differentiation. Alterations in Wnt signaling and reduced ossification could affect the mineral phase of type XIV OI bone, which does not display the hypermineralization common to classical OI types.

Murine data on a new *Tmem38b* cKO mouse displayed detrimental effects on growth and mineralization, with further evidence of reduced calcium calmodulin kinase II-mediated and TGF-β signaling (18). This expansion of our understanding of the mechanism underlying type XIV skeletal pathophysiology provides potential modifying factors and molecular targets in OI. Our studies were limited to osteoblasts from a single OI patient because of the rarity of type XIV OI and the logistical challenge of obtaining bone chip surgical discard. Limited RT-qPCR comparison of patient osteoblasts to additional control supports the results presented for cell-adhesion transcripts (Supplemental Figure 4A-B). Further exploration of cell adhesion and metabolism processes in additional patient or murine models is warranted, to understand whether these are common disrupted pathways among different OI types and their role in the shared mechanism of OI types.

Experimental procedures

Human subjects—This study was approved by the NICHD IRB (Protocol #04-CH-0077). Cells from our type XIV OI patient, a prepubertal male who was age 13 at the time of biopsy, were obtained as part of the diagnostic workup. The donor of healthy control osteoblasts is a sex-matched 10-year-old male at the time of his surgical procedure. The donor previously had septic arthritis resulting in femoral head deformity and required an operative procedure to re-orientate the femur. The control osteoblasts in our study were harvested from the donor's healthy proximal femur. Written, informed consent was obtained from all subjects or their respective guardians (JCM for proband, and MT for control).

Patient bone samples and murine calvarial cells—Primary osteoblasts were derived from surgical discard bone chips of patient and healthy age-matched donor. Bone chips were minced and processed according to the Robey and Termine (65). Bone chips were digested in alpha-minimal essential medium (αMEM, Gibco) with Penicillin-Streptomycin antibiotics (100 units/mL Penicillin; 100 μg/mL Streptomycin, Gibco) and Collagenase P (Roche) for 2 hours at 37° C. After digestion, bone chips were transferred to the culture dish with αMEM media supplemented with 1% Penicillin-Streptomycin and 10% fetal bovine serum (Gem Cell, Gemini Bio) at 37C (8% CO_2) for several weeks until osteoblasts emerged on to the culture dish.

Murine calvarial osteoblasts were isolated from 2–4 days old control (*Tmem38b*$^{fl/fl}$) and mutant (*Runx2Cre;Tmem38b*$^{fl/fl}$) pups (18) as previously described (66). Cells were used at passage 1.

Osteoblast *in vitro* differentiation—Osteoblasts from control and patient were seeded (2×10^5/well) in 6-well plates in triplicates per each timepoint of differentiation (Day 0, Day 7, Day 14, Day 21) in αMEM media supplemented with 10% FBS and 1% Penicillin-Streptomycin. At subconfluency, cells were treated with osteoblast differentiation media containing osteogenic supplements: β-glycerol phosphate disodium salt hydrate (2.5 mM, Sigma), (+)-Sodium L-ascorbate (50 μg/mL, Sigma) and dexamethasone (10 nM, Sigma), with media change every 3 days.

Murine control and mutant calvarial osteoblasts were plated at density 1.5×10^4 /cm^2. The cells were cultured in osteogenic media consisting of α-MEM, 10% FBS, antibiotics, 50 μg/mL L-ascorbic acid (Sigma-Aldrich) and 10 mM β-glycerophosphate (Sigma-Aldrich). Medium was changed three times a week. Harvest was performed at Day 2, 7, 14 and 21. Three independent cell preparations were used for experiments.

RNA extraction and Real-time quantitative PCR (RT-qPCR)

At each timepoint (Day 0, Day 7, Day 14, Day 21) patient and control osteoblasts were harvested and RNA was extracted using RNeasy Mini Kit according to manufacturer's instructions (Qiagen, 74106). RNA concentration was measured by NanoDrop spectrophotometer.

cDNA was synthesized using high-capacity cDNA reverse transcription kit (Applied Biosystems). For each RT-qPCR reaction, 20 ng of cDNA was used. RT-qPCR reaction was carried out on Quant Studio 6 Flex (Applied Biosystems) using TaqMan fast universal PCR master mix. mRNA expression levels of genes were normalized to *B2M* reference gene based on comparative Ct method ($^{\Delta\Delta}$Ct). The TaqMan probes sequences are as follows: *COL1A1* (Hs00164004_m1), *ALPL* (Hs01029144_m1), *IBSP* (Hs00173720_m1), *SPARC* (Hs00234160_m1), *SPP1* (Hs00959010_m1), *DMP1* (Hs00189368_m1), *SOST* (Hs00228820_m1), *RANKL* (Hs00243522_m1), *OPG* (Hs00921369_m1), *PCDHA10* (Hs00258985_s1), *PCDHB7* (Hs00961094_s1), *PCDHB10* (Hs04188974_s1), *PCDHB11* (Hs00946730_s1), *PCDHB12* (Hs04188997_s1), *PCDHB13* (Hs00251745_s1), *PCDHB15* (Hs00251757_s1), *PCDHGA7* (Hs00259352_s1), *PCDHGA12* (Hs01571755_s1), *DCHS1* (Hs01044548_m1), *CLDN1* (Hs00221623_m1), *CADM1* (Hs00942509_m1), *ICAM1* (Hs00164932_m1), *CELSR2* (Hs00154903_m1), *PTPRF* (Hs00160837_m1), *PTPRD* (Hs00369913_m1), *CDH2* (Hs00983056_m1), *CDH4* (Hs00899698_m1), *GJA1* (Hs00748445_s1), *TJP1* (Hs00543811_g1), *CCND2* (Hs00153380_m1), *CCNE1* (Hs01026536_m1), *CCNE2* (Hs00180319_m1), *CCNB1* (Hs01030099_m1), *CCNB2* (Hs01084593_g1), *CTGF* (Hs00170014), *SERPINH1* (Hs00241844_m1), *HEY2* (Hs01012057_m1), *B2M* (Hs00984230_m1) (Applied Biosystems).

For murine studies, total RNA was extracted from osteoblasts after 2, 7, 14 and 21 days of culture in osteogenic medium using Trizol according to the manufacturer's protocol. DNase digestion was performed using the Turbo DNA Free Kit (Applied Biosystems), and RNA integrity was verified on agarose gel. cDNA was synthetized using RT^2 First Strand kit (Applied Biosystems) starting from 1 μg RNA. Reactions were performed on the QuantStudio3 thermocycler (Thermofisher) using PowerUp Syber Green Master Mix (Applied Biosystems), using the following primers: *Gja1* Forward: 5'-TTGACTTCAGCCTCCAAGG-3', *Gja1* Reverse 5'-AATGAAGAGCACCGACAGC-3'; *Tjp1* Forward: 5'GCTAAGAGCACAGCAATGGA, *Tjp1* Reverse: 5'-GCATGTTCAACGTTATCCAT-3'. *Gapdh* was used as reference gene for normalization, and relative expression was calculated using the $^{\Delta\Delta}$Ct method.

Osteoblast mineralization assay by Alizarin Red staining

Osteoblasts from control and patient were seeded in 12-well plates in triplicate and differentiated for 6 weeks in osteoblasts differentiation media (αMEM media, 10% FBS, 1% Penicillin-Streptomycin) supplemented with β-glycerol phosphate disodium salt hydrate (2.5 mM, Sigma), (+)-Sodium L-ascorbate (50 μg/mL, Sigma), dexamethasone (10 nM, Sigma), and recombinant BMP-2 (100 ng/mL, 355-BM, R&D Systems, Minneapolis, MN). At the end point of differentiation, cells were fixed with 4% paraformaldehyde (PFA) for 10 minutes, and then washed with PBS. Fixed cells were stained for 30 minutes with 1% Alizarin Red/2% ethanol (pH 4.1–4.3) at room temperature. Excess dye was washed with distilled water. Stained cultures were photographed for representation. Dye was extracted with extraction buffer (0.5M HCl, 5% SDS) for 10 minutes at room temperature, and the absorbance was read at 405 nm.

RNA sequencing (RNA-Seq) and data analysis

RNA from control and patient osteoblasts at Day 0, Day 7, Day 14, and Day 21 timepoints of osteoblasts differentiation, previously extracted with RNeasy Mini Kit were subject to bulk RNA-Seq transcriptomics. Total RNA samples (~2 μg) were purified with Poly-A extraction, and then used to construct RNA-Seq libraries with specific barcodes using the Illumina TruSeq Stranded mRNA Library Prep Kit. All RNA-Seq libraries were pooled together and sequenced using an Illumina NovaSeq 6000 sequencer to generate approximately 40–50 million 2 × 100 bp reads for each sample. The raw data were demultiplexed and analyzed further using lcdb-wf v1.8rc (lcdb.github.io/lcdb-wf/) according to the following steps: Raw sequence reads were trimmed with cutadapt v3.4 (67) to remove any adapters while performing light quality trimming with parameters '-a AGATCGGAAGAGCACACGTCTGAACTCCAGTCAAAGATCGGAAGAGCGTCGTGTA-GGGAAAGAGTGT-q 20 –minimum-length = 25.' Sequencing library quality was assessed with fastqc v0.11.9 with default parameters. The presence of common sequencing contaminants was evaluated with fastq_screen v0.14.0 with parameters '– subset 100000 –aligner bowtie2.' Trimmed reads were mapped to the Homo sapiens reference genome (GENCODE v28) using STAR v2.7.8 (68) in the one-pass mode with parameters used by the ENCODE long RNA-Seq pipeline: "--outFilterMultimapNmax 20 --alignSJoverhangMin 8 --alignSJDBoverhangMin 1 --outFilterMismatchNmax 999 -outFilterMismatchNoverReadLmax 0.04 --alignIntronMin 20 --alignIntronMax 1000000 -alignMatesGapMax 1000000". Uniquely aligned reads mapping to genes were quantified using the featureCounts program of the subread package v2.0.1 (69) using the Homo sapiens reference (GENCODE v28) annotations. Differential expression was performed using raw counts supplied to DESeq2 v1.28.0 (70) with the following modifications from lfcShrink default parameters: type="ashr" (71) and lfcThreshold=1. A gene was considered differentially expressed if the false discovery rate (FDR) was <0.1 (default for DESeq2 for the statistical test that magnitude of the log2FoldChange is greater than 1 (lfcThreshold=1)). Functional enrichment was performed for GO Biological Process, Cellular Component and Molecular Function using the ClusterProfiler v 3.16.0 (72) function go.enrich. To calculate percentiles for protocadherin genes we performed a transcript per kilobase per million (TPM) normalization using salmon v1.4.0 (73) to correct for gene length and library size, before collapsing to gene-level estimates. Subsequently, we removed all genes with zero reads in all samples, averaged TPM values across replicates and calculated percentiles that were defined as the proportion of genes having lower expression than protocadherin genes.

Western Blot

Osteoblasts from control and patient were seeded in 6 cm plates in triplicate per each timepoint and harvested at Day 0, 7, 14, and 21 of osteoblast differentiation in RIPA buffer containing protease inhibitor cocktail (P8340, Sigma). Cell lysates were sonicated for 5 seconds, centrifuged at 12,000g for 10 minutes and supernatant was transferred to a new tube. To determine protein concentration of samples, Pierce™ BCA Protein Assay Kit (23225, Thermo Fisher) was used according to manufacturer's instructions. Samples were mixed with Laemmli sample buffer (BioRad) and denatured at 95°C for 5 minutes. SDS-PAGE electrophoresis was performed for 1.5 hours at 150 Volt using 4–15% gradient gel (Criterion™ TGX Stain-Free™ Precast Gels, Bio-Rad Laboratories). Protein transfer was performed for 7 minutes at 20 Volt on iBlot 2 Dry Blotting System (Invitrogen) using nitrocellulose transfer membrane (iBlot™ 2 Transfer Stacks, Invitrogen). Control and mutant samples were run together in the same electrode reservoir, treated with the same buffers at the same time, and transferred back-to-back in the same chamber for the Western blots. After protein transfer, the membrane was incubated in Tris-buffered saline (TBS) containing 0.1% Tween-20 (Sigma) and 5% bovine serum albumin (BSA, Gemini Bio) for 1 hour, following overnight incubation with primary antibody at 4°C. Dilutions of primary antibodies are as follows: Cx43 (3512S) 1:1000; ZO-1 (13663S) 1:1000; Cyclin D1 (92G2) 1:1000, Cyclin D2 (3741S) 1:1000, Cyclin D3 (DCS22) 1:1000, Cyclin B1 (D5C10, XP(R)) 1:1000, PTK7 (25618S) 1:1000, Paxillin (12065S) 1:1000, Jagged1 (2620T) 1:1000, CTGF (10095S) 1:500, DRP1 (5391T) 1:1000, Mitofusin-2 (11925S) 1:1000, GAPDH (D4C6R) 1:1000, GAPDH (D16H11, XP(R)) 1:1000 Cell Signaling; HSP47 (ADI-SPA-470) 1:1000, Enzo Life Sciences. The following day, the membrane was washed 3 times for 10 minutes in washing buffer (TBS-Tween), and then incubated with secondary antibody (IRDye® 800 CW anti-mouse, IRDye® 680 RD anti-rabbit, Li-COR; 1:10,000) for 1 hour. After washing, the membrane was developed using LI-COR Odyssey® CLx Western Blot imager.

Immunocytochemistry

Control and patient osteoblasts were seeded in 8-well glass chamber slide. Cells were fixed with 4% PFA for 15 minutes followed by PBS washes x3 for 5 minutes. Blocking was performed for 1 hour in buffer containing 5% normal goat serum (Jackson Immuno Research) and 0.1% Triton in PBS. Incubation with primary antibody was for 2 hours at room temperature (Cx43 (3512S) 1:100, ZO-1 (13663S) 1:100, Cell Signaling; Ki67 (ab16667) 1:300, Abcam; HSP47 (ADI-SPA-470) 1:500, Enzo Life Sciences). After PBS washes, cells were incubated with secondary antibodies (Alexa Fluor™ 555 donkey anti-mouse IgG; Alexa Fluor™ 488 goat anti-rabbit IgG, Invitrogen; 1:200) for 1 hour. Cells were washed with PBS, and counterstained with DAPI (1ug/mL) for 10 minutes. Slides were mounted with Vectashield® antifade mounting medium (H-1000, Vector Laboratories) and covered with cover slips. Images were taken with Zeiss LSM 710 Confocal Microscope. For Ki67 staining, 10 images, with approximately 900 cells in total per genotype, were analyzed.

For murine experiments, 2×10^4 calvarial osteoblasts per well were plated on sterile glass coverslips (Marienfeld) in 24 well plate. At Day 2 cells were fixed with 4% PFA for 10 minutes, permeabilized with 0.1% Triton™ X-100 for 15 minutes and blocked with 2% BSA for 45 minutes at room temperature. The cells were then labelled overnight at 4°C with anti ZO-1 antibody (40–2200, Invitrogen) at 5 μg/mL in 1% BSA, or with anti Cx43 antibody (35–5000, Invitrogen) at 1:500 dilution in 2% BSA. Following PBS washes, cells were incubated with secondary antibody (AlexaFluor 488 or 546 conjugated F(ab’) fragment anti- rabbit IgG, Immunological Sciences) diluted 1:2000 in 1% BSA, 0.3% Triton™ X-100 in PBS for 2 hours at room temperature. Nuclei were stained with DAPI and images were acquired by confocal microscope TCS SP8 (Leica). The total area of signal per cell was measured by the Leica software LAS 4.5.

MitoTEMPO treatment and measurement of mitochondrial ROS

Control and patient osteoblasts were seeded in 8-well glass chamber slides. To evaluate the production of superoxide, the cells were stained with MitoSOX™ Red (Invitrogen, M36008), a novel fluorogenic dye for highly selective detection of superoxide in the mitochondria of live cells. Once in the mitochondria, MitoSOX™ Red reagent is oxidized only by superoxide and exhibits red fluorescence. Live cells were incubated with 5 μM of MitoSOX™ Red (Invitrogen, M36008) for 15 minutes in a humidified incubator, followed by three consecutive PBS washes. Images of MitoSOX staining were taken with a Zeiss LSM 710 Confocal Microscope with on-stage incubator. In parallel, control and patient osteoblasts were stimulated with 50 μM of MitoTEMPO (SML0737, Sigma) for 24 hours, which is a mitochondrially targeted antioxidant and a specific scavenger of mitochondrial superoxide, followed by MitoSOX staining and liveimaging of cells. The levels of mt-ROS were measured by seeding the control and patient osteoblasts in a 96-well plate overnight. Then, the cells were stained with MitoSOX and the fluorescence intensity, which is directly proportional to the level of mtROS in the cell, was measured with the EnSpire® Multimode Plate Reader (PerkinElmer).

BrdU proliferation assay

Control and patient osteoblasts were seeded in a 96-well plate at 20,000 cells per well and treated with BrdU reagent overnight. The protocol was performed according to manufacturer's instructions (BrdU Cell Proliferation Assay Kit, 6813, Cell Signaling).

Electron microscopy

Control and patient osteoblasts were seeded in 6-well plates and at subconfluent level were fixed with EM fixative solution (2% glutaraldehyde in 0.1M cacodylate buffer, pH 7.4) for 1 hour at room temperature followed by overnight fixation at 4°C. The following day, EM fixative was replaced with PBS. In the NCI/NIH electron microscopy core facility, the cell plates were processed and embedded at room temperature in a fume hood. Following fixation, the cells were washed 2 times for 10 minutes in cacodylate buffer before post-fixation of 1 hour in osmium tetroxide (1% v/v). The cells were then washed 2 times with water and 1 time with acetate buffer (0.1M, pH 4.5) before *en bloc* stain in 0.5% w/v uranyl acetate (0.5% v/v) in acetate buffer (0.1M, pH 4.5) for 1 hour. The cells were dehydrated with multiple washes of EM grade ethanol at 35%, 50%, 75%, 95%, and 100%, consecutively. The cells were then washed with pure epoxy resin (Poly/Bed® 812, Polysciences, Inc.) overnight. The following day the cells were washed with pure resin prior to embedding. Immediately after embedding, the cell plates were placed in a 55°C oven to cure for 48 hours. The resin blocks were separated from the plate and examined under an inverted microscope to select an area with considerable cell number. The preferred area was removed from the block, trimmed and thin sectioned using an ultramicrotome equipped with a diamond knife. The thin sections were mounted onto copper mesh grids for counter staining with uranyl acetate and lead citrate. The grids were then carbon coated in a vacuum evaporator. Once carbon coated the grids are prepared to be scanned and imaged. The entire grid was scanned, with detailed examination of 100 cells, after which representative images were taken. The Hitachi Electron microscope (H7650) operated at 80kv with a CCD camera captured the digital images.

Antibody array-based proteomics

Proteomics was conducted using the RayBio® Label-Based (L-Series) Human Antibody Array L-6000 Glass Slide Kit, a combination of 12 different human arrays by RayBiotech Life, Inc. The array simultaneously detected the relative expression of 6000 human proteins including cytokines, chemokines, adipokines, extracellular matrix proteins, growth factors, angiogenic factors, proteases, enzymes, soluble and transmembrane receptors and transport proteins, adhesion molecules and other proteins using 100 μg of cell lysates from control and patient osteoblasts at Day 0 and Day 14 of differentiation. For interpretation of results, three positive controls of standardized biotinylated IgG were used in each array. The positive control intensities are the same for each sub-array, which allows normalization based upon the relative fluorescence signal responses to a known control. Once fluorescence intensity data are obtained, the background is subtracted, and data normalized to the positive control signals. To normalize signal intensity data, one sub-array is defined as "reference" to which the other arrays are normalized. The top upregulated and top downregulated proteins with > 2 fold change were further shown. The functions were assigned to relevant proteins using the Metascape software (74).

Statistics

For statistical analysis we used a 2-tailed Student's t test. Data are presented as means ± SEM. A value of $P < 0.05$ was considered significant.

Supplementary Material

Refer to Web version on PubMed Central for supplementary material.

Funding

The following grants supported our study: NICHD IRP funding to Joan C. Marini, ZIA HD000408–38, and Italian Ministry of Education, University and Research (MIUR) [Dipartimenti di Eccellenza (2018–2022)] to Antonella Forlino.

Data availability

Full electronic RNA-Seq and proteomic data will be available in the database of Genotypes and Phenotypes (dbGaP).

Abbreviations

OI	Osteogenesis Imperfecta
COL1A1	collagen type I alpha 1 gene
COL1A2	collagen type I alpha 2 gene
TMEM38B	transmembrane protein 38B
ER	endoplasmic reticulum
TRIC-B	trimeric intracellular cation channel type B
IP3R	inositol 1, 4, 5 trisphosphate receptor
BMDD	bone mineral density distribution
BMD	bone mineral density

DXA	dual-energy X-ray absorptiometry
CT	computerized tomography
ALPL	alkaline phosphatase
IBSP	integrin binding sialoprotein
SPP1	secreted phosphoprotein 1
SPARC	secreted protein acidic and cysteine rich
DMP1	dentin matrix acidic phosphoprotein 1
SOST	sclerostin
RANKL	receptor activator of nuclear factor kappa B ligand
OPG	osteoprotegerin
CAMs	cell adhesion molecules
DEGs	differentially expressed genes
PCDHA10	protocadherin alpha 10
PCDHB7	protocadherin beta 7
PCDHB10	protocadherin beta 10
PCDHB11	protocadherin beta 11
PCDHB12	protocadherin beta 12
PCDHB13	protocadherin beta 13
PCDHB15	protocadherin beta 15
PCDHGA7	protocadherin gamma subfamily A 7
PCDHGA12	protocadherin gamma subfamily A 12
DCHS1	protocadherin 16
CLDN1	claudin 1
CADM1	cell adhesion molecule-1
ICAM1	intracellular adhesion molecule-1
CELSR2	cadherin EGF LAG seven-pass G-type receptor 2
PTPRF	protein tyrosine phosphatase receptor type F
PTPRD	protein tyrosine phosphatase receptor type D
CDH2	cadherin-2

CDH4	cadherin-4
GJA1	gap junction protein alpha 1
Cx43	connexin 43
TJP1	tight junction protein 1
ZO-1	zonula occludens-1
ROS	reactive oxygen species
ECM	extracellular matrix
PTK7	protein tyrosine kinase 7
PXN	paxillin
JAG1	Jagged1
CCND2	cyclin D2
CCNE1	cyclin E1
CCNE2	cyclin E2
CCNB1	cyclin B1
CCNB2	cyclin B2
CTGF	connective tissue growth factor
HSP47	heat shock protein 47
SERPINH1	serpin family H member 1
ER-MCSs	ER mitochondria contact sites
DRP1	dynamin-related protein 1
MFN2	mitofusin-2
mt-ROS	mitochondrial reactive oxygen species
FAT4	FAT atypical cadherin 4
LPS	lipopolysaccharide
OXPHOS	oxidative phosphorylation
TNBC	triple-negative breast cancer
BMP-2	bone morphogenic protein 2
GO	Gene Ontology

References

1. Jovanovic M, Guterman-Ram G, Marini JC. Osteogenesis imperfecta: mechanisms and signaling pathways connecting classical and rare OI types. Endocrine reviews. 2022;43(1):61–90. [PubMed: 34007986]
2. Besio R, Chow CW, Tonelli F, Marini JC, Forlino A. Bone biology: insights from osteogenesis imperfecta and related rare fragility syndromes. The FEBS journal. 2019;286(15):3033–3056. [PubMed: 31220415]
3. Yazawa M, Ferrante C, Feng J, Mio K, Ogura T, Zhang M, Lin P-H, Pan Z, Komazaki S, Kato K. TRIC channels are essential for Ca2+ handling in intracellular stores. Nature. 2007;448(7149):78–82. [PubMed: 17611541]
4. Cabral WA, Ishikawa M, Garten M, Makareeva EN, Sargent BM, Weis M, Barnes AM, Webb EA, Shaw NJ, Ala-Kokko L. Absence of the ER cation channel TMEM38B/TRIC-B disrupts intracellular calcium homeostasis and dysregulates collagen synthesis in recessive osteogenesis imperfecta. PLoS genetics. 2016;12(7):e1006156.
5. Jansen G, Määttänen P, Denisov AY, Scarffe L, Schade B, Balghi H, Dejgaard K, Chen LY, Muller WJ, Gehring K. An interaction map of endoplasmic reticulum chaperones and foldases. Molecular & Cellular Proteomics. 2012;11(9):710–723. [PubMed: 22665516]
6. Michalak M, Groenendyk J, Szabo E, Gold LI, Opas M. Calreticulin, a multi-process calciumbuffering chaperone of the endoplasmic reticulum. Biochemical Journal. 2009;417(3):651–666. [PubMed: 19133842]
7. Volodarsky M, Markus B, Cohen I, Staretz-Chacham O, Flusser H, Landau D, Shelef I, Langer Y, Birk OS. A Deletion Mutation in TMEM 38 B Associated with Autosomal Recessive Osteogenesis Imperfecta. Human mutation. 2013;34(4):582–586. [PubMed: 23316006]
8. Shaheen R, Alazami AM, Alshammari MJ, Faqeih E, Alhashmi N, Mousa N, Alsinani A, Ansari S, Alzahrani F, Al-Owain M. Study of autosomal recessive osteogenesis imperfecta in Arabia reveals a novel locus defined by TMEM38B mutation. Journal of medical genetics. 2012;49(10):630–635. [PubMed: 23054245]
9. Rubinato E, Morgan A, D'Eustacchio A, Pecile V, Gortani G, Gasparini P, Faletra F. A novel deletion mutation involving TMEM38B in a patient with autosomal recessive osteogenesis imperfecta. Gene. 2014;545(2):290–292. [PubMed: 24835313]
10. Lv F, Xu X-j, Wang J-y, Liu Y, Wang J-w, Song L-j, Song Y-w, Jiang Y, Wang O, Xia W-b. Two novel mutations in TMEM38B result in rare autosomal recessive osteogenesis imperfecta. Journal of human genetics. 2016;61(6):539–545. [PubMed: 26911354]
11. Webb EA, Balasubramanian M, Fratzl-Zelman N, Cabral WA, Titheradge H, Alsaedi A, Saraff V, Vogt J, Cole T, Stewart S. Phenotypic spectrum in osteogenesis imperfecta due to mutations in TMEM38B: unraveling a complex cellular defect. The Journal of Clinical Endocrinology & Metabolism. 2017;102(6):2019–2028. [PubMed: 28323974]
12. Sukhanov N, Vainshtein A, Eshed-Eisenbach Y, Peles E. Differential Contribution of Cadm1–Cadm3 Cell Adhesion Molecules to Peripheral Myelinated Axons. Journal of Neuroscience. 2021;41(7):1393–1400. [PubMed: 33397712]
13. Deans MR, Krol A, Abraira VE, Copley CO, Tucker AF, Goodrich LV. Control of neuronal morphology by the atypical cadherin Fat3. Neuron. 2011;71(5):820–832. [PubMed: 21903076]
14. Seiradake E, del Toro D, Nagel D, Cop F, Härtl R, Ruff T, Seyit-Bremer G, Harlos K, Border EC, Acker-Palmer A. FLRT structure: balancing repulsion and cell adhesion in cortical and vascular development. Neuron. 2014;84(2):370–385. [PubMed: 25374360]
15. Gumbiner BM. Cell adhesion: the molecular basis of tissue architecture and morphogenesis. Cell. 1996;84(3):345–357. [PubMed: 8608588]
16. Itoh M, Nagafuchi A, Moroi S, Tsukita S. Involvement of ZO-1 in cadherin-based cell adhesion through its direct binding to α catenin and actin filaments. The Journal of cell biology. 1997;138(1):181–192. [PubMed: 9214391]
17. Kotini M, Barriga EH, Leslie J, Gentzel M, Rauschenberger V, Schambony A, Mayor R. Gap junction protein Connexin-43 is a direct transcriptional regulator of N-cadherin in vivo. Nature communications. 2018;9(1):1–17.

18. Besio R, Contento BM, Garibaldi N, Filibian M, Sonntag S, Shmerling D, Tonelli F, Biggiogera M, Brini M, Salmaso A, Jovanovic M, Marini JC, Rossi A, Forlino A. CaMKII inhibition due to TRIC-B loss-of-function dysregulates SMAD signalling in osteogenesis imperfecta. Matrix Biol. 2023.
19. Park S-K, Lee H-S, Lee S-T. Characterization of the human full-length PTK7 cDNA encoding a receptor protein tyrosine kinase-like molecule closely related to chick KLG. The Journal of Biochemistry. 1996;119(2):235–239. [PubMed: 8882711]
20. Turner CE. Paxillin and focal adhesion signalling. Nature cell biology. 2000;2(12):E231–E236. [PubMed: 11146675]
21. Zanotti S, Canalis E. Notch signaling and the skeleton. Endocrine reviews. 2016;37(3):223–253. [PubMed: 27074349]
22. Takeichi M. The cadherins: cell-cell adhesion molecules controlling animal morphogenesis. Development. 1988;102(4):639–655. [PubMed: 3048970]
23. Resende RR, Andrade LM, Oliveira AG, Guimarães ES, Guatimosim S, Leite MF. Nucleoplasmic calcium signaling and cell proliferation: calcium signaling in the nucleus. Cell communication and signaling. 2013;11:1–7. [PubMed: 23289948]
24. Ito S, Nagata K. Roles of the endoplasmic reticulum–resident, collagen-specific molecular chaperone Hsp47 in vertebrate cells and human disease. Journal of Biological Chemistry. 2019;294(6):2133–2141. [PubMed: 30541925]
25. Abrisch RG, Gumbin SC, Wisniewski BT, Lackner LL, Voeltz GK. Fission and fusion machineries converge at ER contact sites to regulate mitochondrial morphology. Journal of Cell Biology. 2020;219(4).
26. Hartsock A, Nelson WJ. Adherens and tight junctions: structure, function and connections to the actin cytoskeleton. Biochimica et Biophysica Acta (BBA)-Biomembranes. 2008;1778(3):660–669. [PubMed: 17854762]
27. Takeichi M. Cadherin cell adhesion receptors as a morphogenetic regulator. Science. 1991;251(5000):1451–1455. [PubMed: 2006419]
28. Marie PJ, Haÿ E, Modrowski D, Revollo L, Mbalaviele G, Civitelli R. Cadherin-mediated cell–cell adhesion and signaling in the skeleton. Calcified tissue international. 2014;94(1):46–54. [PubMed: 23657489]
29. Marie PJ. Role of N-cadherin in bone formation. Journal of cellular physiology. 2002;190(3):297305.
30. Liu Q, Babb S, Novince Z, Doedens A, Marrs J, Raymond P. Differential expression of cadherin-2 and cadherin-4 in the developing and adult zebrafish visual system. Visual neuroscience. 2001;18(6):923–933. [PubMed: 12020083]
31. Cappello S, Gray MJ, Badouel C, Lange S, Einsiedler M, Srour M, Chitayat D, Hamdan FF, Jenkins ZA, Morgan T. Mutations in genes encoding the cadherin receptor-ligand pair DCHS1 and FAT4 disrupt cerebral cortical development. Nature genetics. 2013;45(11):1300–1308. [PubMed: 24056717]
32. Crespo-Enriquez I, Hodgson T, Zakaria S, Cadoni E, Shah M, Allen S, Al-Khishali A, Mao Y, Yiu A, Petzold J. Dchs1-Fat4 regulation of osteogenic differentiation in mouse. Development. 2019;146(14):dev176776.
33. Stewart K, Uetani N, Hendriks W, Tremblay ML, Bouchard M. Inactivation of LAR family phosphatase genes Ptprs and Ptprf causes craniofacial malformations resembling Pierre-Robin sequence. Development. 2013;140(16):3413–3422. [PubMed: 23863482]
34. Sarhan AR, Patel TR, Cowell AR, Tomlinson MG, Hellberg C, Heath JK, Cunningham DL, Hotchin NA. LAR protein tyrosine phosphatase regulates focal adhesions through CDK1. Journal of cell science. 2016;129(15):2962–2971. [PubMed: 27352860]
35. Inoue T, Hagiyama M, Enoki E, Sakurai MA, Tan A, Wakayama T, Iseki S, Murakami Y, Fukuda K, Hamanishi C. Cell adhesion molecule 1 is a new osteoblastic cell adhesion molecule and a diagnostic marker for osteosarcoma. Life sciences. 2013;92(1):91–99. [PubMed: 23142238]
36. Lavigne P, Benderdour M, Shi Q, Lajeunesse D, Fernandes JC. Involvement of ICAM-1 in bone metabolism: a potential target in the treatment of bone diseases? Expert opinion on biological therapy. 2005;5(3):313–320. [PubMed: 15833069]

37. Pancho A, Aerts T, Mitsogiannis MD, Seuntjens E. Protocadherins at the crossroad of signaling pathways. Frontiers in Molecular Neuroscience. 2020;13:117. [PubMed: 32694982]
38. Alshbool FZ, Mohan S. Differential expression of claudin family members during osteoblast and osteoclast differentiation: Cldn-1 is a novel positive regulator of osteoblastogenesis. PloS one. 2014;9(12):e114357.
39. Einarsdottir E, Grauers A, Wang J, Jiao H, Escher SA, Danielsson A, Simony A, Andersen M, Christensen SB, Åkesson K. CELSR2 is a candidate susceptibility gene in idiopathic scoliosis. PloS one. 2017;12(12):e0189591.
40. Peradziryi H, Tolwinski NS, Borchers A. The many roles of PTK7: a versatile regulator of cell–cell communication. Archives of biochemistry and biophysics. 2012;524(1):71–76. [PubMed: 22230326]
41. Fu P, Epshtein Y, Ramchandran R, Mascarenhas JB, Cress AE, Jacobson J, Garcia JG, Natarajan V. Essential role for paxillin tyrosine phosphorylation in LPS-induced mitochondrial fission, ROS generation and lung endothelial barrier loss. Scientific Reports. 2021;11(1):17546. [PubMed: 34475475]
42. Kopan R, Ilagan MXG. The canonical Notch signaling pathway: unfolding the activation mechanism. Cell. 2009;137(2):216–233. [PubMed: 19379690]
43. Song S, Babicheva A, Zhao T, Ayon RJ, Rodriguez M, Rahimi S, Balistrieri F, Harrington A, Shyy JYJ, Thistlethwaite PA. Notch enhances Ca2+ entry by activating calcium-sensing receptors and inhibiting voltage-gated K+ channels. American Journal of Physiology-Cell Physiology. 2020.
44. Lindner V, Booth C, Prudovsky I, Small D, Maciag T, Liaw L. Members of the Jagged/Notch gene families are expressed in injured arteries and regulate cell phenotype via alterations in cell matrix and cell-cell interaction. The American journal of pathology. 2001;159(3):875–883. [PubMed: 11549580]
45. Luo Z, Shang X, Zhang H, Wang G, Massey PA, Barton SR, Kevil CG, Dong Y. Notch signaling in osteogenesis, osteoclastogenesis, and angiogenesis. The American journal of pathology. 2019;189(8):1495–1500. [PubMed: 31345466]
46. Morello R, Bertin TK, Chen Y, Hicks J, Tonachini L, Monticone M, Castagnola P, Rauch F, Glorieux FH, Vranka J. CRTAP is required for prolyl 3-hydroxylation and mutations cause recessive osteogenesis imperfecta. Cell. 2006;127(2):291–304. [PubMed: 17055431]
47. Chipman SD, Sweet HO, McBride DJ Jr, Davisson MT, Marks SC Jr, Shuldiner AR, Wenstrup RJ, Rowe DW, Shapiro JR. Defective pro alpha 2 (I) collagen synthesis in a recessive mutation in mice: a model of human osteogenesis imperfecta. Proceedings of the National Academy of Sciences. 1993;90(5):1701–1705.
48. Zimmerman SM, Dimori M, Heard-Lipsmeyer ME, Morello R. The osteocyte transcriptome is extensively dysregulated in mouse models of osteogenesis imperfecta. JBMR plus. 2019;3(7):e10171.
49. Bini L, Schvartz D, Carnemolla C, Besio R, Garibaldi N, Sanchez J-C, Forlino A, Bianchi L. Intracellular and extracellular markers of lethality in osteogenesis imperfecta: a quantitative proteomic approach. International Journal of Molecular Sciences. 2021;22(1):429. [PubMed: 33406681]
50. Campbell HK, Maiers JL, DeMali KA. Interplay between tight junctions & adherens junctions. Experimental cell research. 2017;358(1):39–44. [PubMed: 28372972]
51. Siliciano J, Goodenough DA. Localization of the tight junction protein, ZO-1, is modulated by extracellular calcium and cell-cell contact in Madin-Darby canine kidney epithelial cells. The Journal of cell biology. 1988;107(6):2389–2399. [PubMed: 3058722]
52. Lurtz MM, Louis CF. Intracellular calcium regulation of connexin43. American Journal of Physiology-Cell Physiology. 2007;293(6):C1806–C1813. [PubMed: 17898133]
53. Lecanda F, Warlow PM, Sheikh S, Furlan F, Steinberg TH, Civitelli R. Connexin43 deficiency causes delayed ossification, craniofacial abnormalities, and osteoblast dysfunction. The Journal of cell biology. 2000;151(4):931–944. [PubMed: 11076975]
54. Laing JG, Chou BC, Steinberg TH. ZO-1 alters the plasma membrane localization and function of Cx43 in osteoblastic cells. Journal of cell science. 2005;118(10):2167–2176. [PubMed: 15855237]

55. Safadi FF, Xu J, Smock SL, Kanaan RA, Selim AH, Odgren PR, Marks SC Jr, Owen TA, Popoff SN. Expression of connective tissue growth factor in bone: its role in osteoblast proliferation and differentiation in vitro and bone formation in vivo. Journal of cellular physiology. 2003;196(1):51–62. [PubMed: 12767040]
56. Hendesi H, Barbe MF, Safadi FF, Monroy MA, Popoff SN. Integrin mediated adhesion of osteoblasts to connective tissue growth factor (CTGF/CCN2) induces cytoskeleton reorganization and cell differentiation. PloS one. 2015;10(2):e0115325.
57. Ivkovic S, Yoon BS, Popoff SN, Safadi FF, Libuda DE, Stephenson RC, Daluiski A, Lyons KM. Connective tissue growth factor coordinates chondrogenesis and angiogenesis during skeletal development. 2003.
58. Prinz WA, Toulmay A, Balla T. The functional universe of membrane contact sites. Nature Reviews Molecular Cell Biology. 2020;21(1):7–24. [PubMed: 31732717]
59. Booth DM, Enyedi B, Geiszt M, Várnai P, Hajnóczky G. Redox nanodomains are induced by and control calcium signaling at the ER-mitochondrial interface. Molecular cell. 2016;63(2):240–248. [PubMed: 27397688]
60. Gorrell L, Makareeva E, Omari S, Otsuru S, Leikin S. ER, Mitochondria, and ISR Regulation by mtHSP70 and ATF5 upon Procollagen Misfolding in Osteoblasts. Advanced Science. 2022;9(29):2201273.
61. Gremminger VL, Jeong Y, Cunningham RP, Meers GM, Rector RS, Phillips CL. Compromised exercise capacity and mitochondrial dysfunction in the osteogenesis imperfecta murine (oim) mouse model. Journal of Bone and Mineral Research. 2019;34(9):1646–1659. [PubMed: 30908713]
62. Moffatt P, Boraschi-Diaz I, Bardai G, Rauch F. Muscle transcriptome in mouse models of osteogenesis imperfecta. Bone. 2021;148:115940.
63. Urra FA, Muñoz F, Córdova-Delgado M, Ramírez MP, Peña-Ahumada B, Rios M, Cruz P, Ahumada-Castro U, Bustos G, Silva-Pavez E. FR58P1a; a new uncoupler of OXPHOS that inhibits migration in triple-negative breast cancer cells via Sirt1/AMPK/β1-integrin pathway. Scientific reports. 2018;8(1):13190. [PubMed: 30181620]
64. Bianchi L, Gagliardi A, Maruelli S, Besio R, Landi C, Gioia R, Kozloff KM, Khoury BM, Coucke PJ, Symoens S. Altered cytoskeletal organization characterized lethal but not surviving Brtl+/− mice: insight on phenotypic variability in osteogenesis imperfecta. Human molecular genetics. 2015;24(21):6118–6133. [PubMed: 26264579]
65. Robey PG, Termine JD. Human bone cellsin vitro. Calcified tissue international. 1985;37(5):453–460.
66. Garibaldi N, Contento BM, Babini G, Morini J, Siciliani S, Biggiogera M, Raspanti M, Marini JC, Rossi A, Forlino A. Targeting cellular stress in vitro improves osteoblast homeostasis, matrix collagen content and mineralization in two murine models of osteogenesis imperfecta. Matrix Biology. 2021;98:1–20. [PubMed: 33798677]
67. Martin M. Cutadapt removes adapter sequences from high-throughput sequencing reads. EMBnet journal. 2011;17(1):10–12.
68. Dobin A, Davis CA, Schlesinger F, Drenkow J, Zaleski C, Jha S, Batut P, Chaisson M, Gingeras TR. STAR: ultrafast universal RNA-seq aligner. Bioinformatics. 2013;29(1):15–21. [PubMed: 23104886]
69. Liao Y, Smyth GK, Shi W. The Subread aligner: fast, accurate and scalable read mapping by seedand-vote. Nucleic acids research. 2013;41(10):e108–e108. [PubMed: 23558742]
70. Love MI, Huber W, Anders S. Moderated estimation of fold change and dispersion for RNA-seq data with DESeq2. Genome biology. 2014;15(12):1–21.
71. Stephens M. False discovery rates: a new deal. Biostatistics. 2017;18(2):275–294. [PubMed: 27756721]
72. Wu T, Hu E, Xu S, Chen M, Guo P, Dai Z, Feng T, Zhou L, Tang W, Zhan L. clusterProfiler 4.0: A universal enrichment tool for interpreting omics data. The Innovation. 2021;2(3):100141.
73. Patro R, Duggal G, Love M, Irizarry R, Kingsford C. Salmon: fast and bias-aware quantification of transcript expression using dual-phase inference. Salmon: fast and bias-aware quantification of transcript expression using dual-phase inference.

74. Zhou Y, Zhou B, Pache L, Chang M, Khodabakhshi AH, Tanaseichuk O, Benner C, Chanda SK. Metascape provides a biologist-oriented resource for the analysis of systems-level datasets. Nature communications. 2019;10(1):1–10.

Highlights

- Deletion of *TMEM38B* causes downregulation and disruption of cell-cell adhesion processes in type XIV OI osteoblasts.
- Gap and tight junctions are decreased in human and murine *TMEM38B*-null osteoblasts, emphasizing a role of TRIC-B across the different species.
- Cell proliferation and cell cycle are slower in the absence of *TMEM38B*.
- *TMEM38B*-null osteoblasts exhibit changes in mitochondrial morphology, together with altered fusion/fission markers and increased mt-ROS production, which is the first evidence of disrupted mitochondrial function in human recessive OI.
- TRIC-B deletion may reveal possible causal link between disrupted mitochondrial metabolism and cell adhesion.

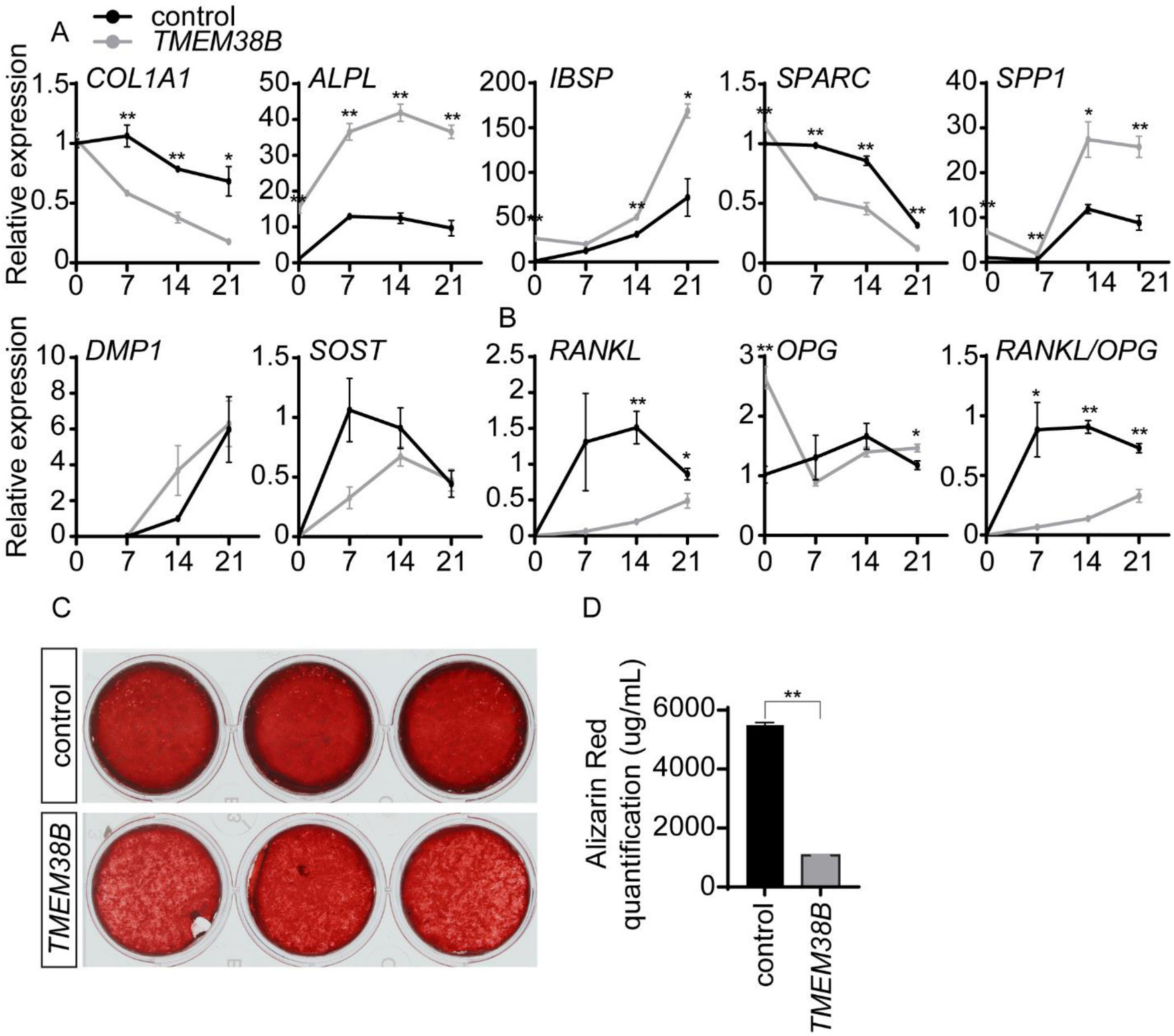

Figure 1.

Altered differentiation and mineralization of human *TMEM38B*-null osteoblasts. A. mRNA expression levels of osteoblast marker genes *COL1A1*, *ALPL*, *IBSP*, *SPARC*, *SPP1*, *DMP1*, *SOST* in control and human *TMEM38B*-null osteoblasts at Day 0, 7, 14, and 21 of differentiation by RT-qPCR analysis. B. mRNA expression levels of osteoblastic genes, affecting osteoclast differentiation, *RANKL*, *OPG* and ratio of *RANKL*/*OPG* in control and human *TMEM38B*-null osteoblasts at Day 0, 7, 14, and 21 of differentiation by RT-qPCR analysis. Expression was normalized to control mRNA expression at Day 0 of osteoblasts differentiation and evaluated by $^{\Delta\Delta}$Ct method. C. Alizarin Red staining of 6 weeks differentiated control and human *TMEM38B*-null osteoblasts. D. Quantification of Alizarin Red staining by hydrochloric acid extraction. Data are presented as means ± SEM. *P < 0.05, **P < 0.01.

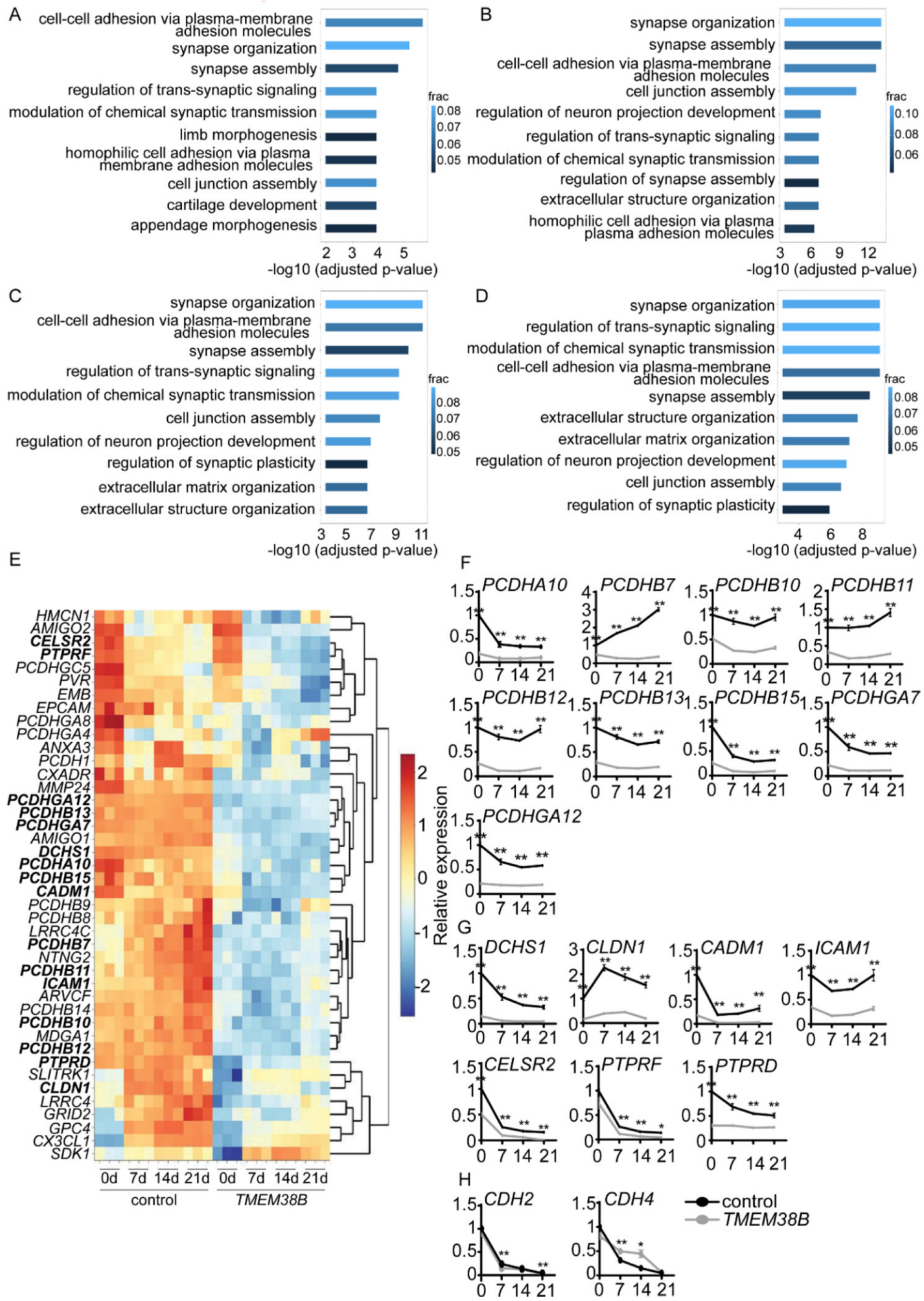

Figure 2.

Downregulated cell-cell adhesion process in human *TMEM38B*-null osteoblasts revealed by RNA-Seq. Functional enrichment analysis showing the top 10 enriched Gene Ontology terms in the Biological Process ontology within downregulated genes in human *TMEM38B*-null osteoblasts compared to control osteoblasts at A) Day 0, B) Day 7, C) Day 14, and D) Day 21 of differentiation. Color depicts the proportion of downregulated genes that were annotated with the GO term. E. Heatmap with normalized counts of adhesion genes from downregulated “cell-cell adhesion via plasma membrane adhesion molecules” GO pathway. mRNA expression level of F) clustered protocadherins and G) adhesion genes with a function in bone, extracted from E) heatmap and evaluated by RT-qPCR analysis at Day 0, 7, 14 and 21 of differentiation in control and human *TMEM38B*-null osteoblasts. H. mRNA expression level of cadherin-2 and −4 at Day 0, 7, 14 and 21 of differentiation in control and human *TMEM38B*-null osteoblasts by RT-qPCR. Expression was normalized to control mRNA expression at Day 0 of osteoblasts differentiation and evaluated by $^{\Delta\Delta}$Ct method. Data are presented as means ± SEM. *P < 0.05, **P < 0.01.

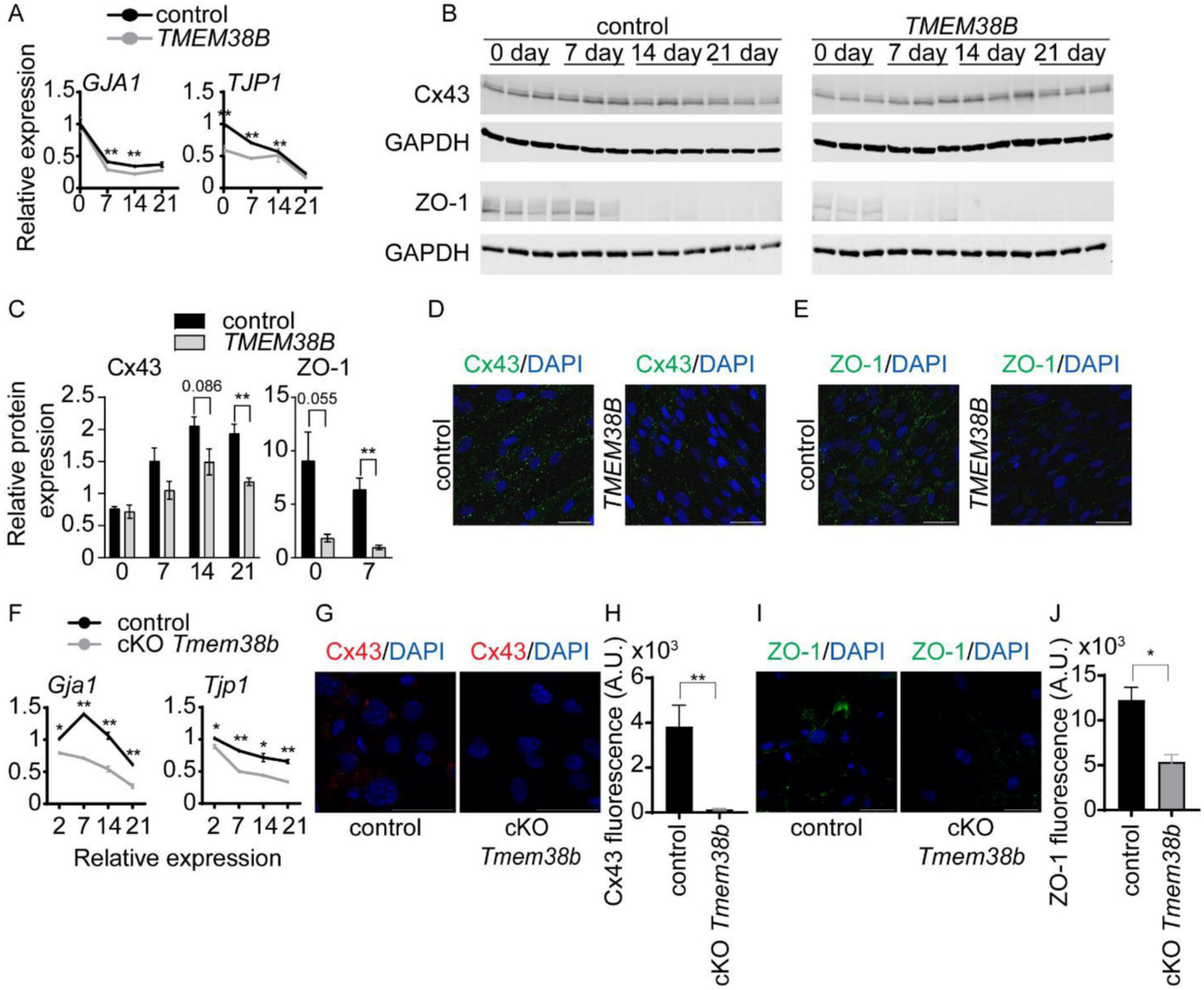

Figure 3.

Gap and tight junction are affected by absence of *TMEM38B* in osteoblasts. A. mRNA expression level of *GJA1*, a gap junction protein, and *TJP1*, a tight junction protein, in control and human *TMEM38B*-null osteoblasts by RT-qPCR at Day 0, 7, 14, and 21 of differentiation. Expression was normalized to control mRNA expression at Day 0 of osteoblasts differentiation and evaluated by $^{\Delta\Delta}$Ct method. B. Western blots of Cx43 and ZO-1 proteins in control and human *TMEM38B*-null osteoblasts at Day 0, 7, 14, and 21 of differentiation. GAPDH was used as a loading control. C. Quantification of Cx43 and ZO-1 protein levels normalized to GAPDH. Immunocytochemistry of D) Cx43 and E) ZO-1 proteins in control and human *TMEM38B*-null osteoblasts. DAPI was used as a counterstain. Scale bars, 50 μm. F. mRNA expression level of *Gja1* and *Tjp1* in murine control and cKO *Tmem38b* osteoblasts at Day 2, 7, 14, and 21 of differentiation. Expression was evaluated by $^{\Delta\Delta}$Ct method. G. Immunocytochemistry of Cx43 protein in control and murine cKO *Tmem38b* osteoblasts at Day 2. DAPI was used as a counterstain. Scale bars, 50 μm. H. Quantification of Cx43 fluorescence signal. I. Immunocytochemistry of ZO-1 protein in murine control and cKO *Tmem38b* osteoblasts at Day 2. DAPI was used as a counterstain. Scale bars, 50 μm. H. Quantification of ZO-1 fluorescence signal. Data are presented as means ± SEM. *P < 0.05, **P < 0.01.

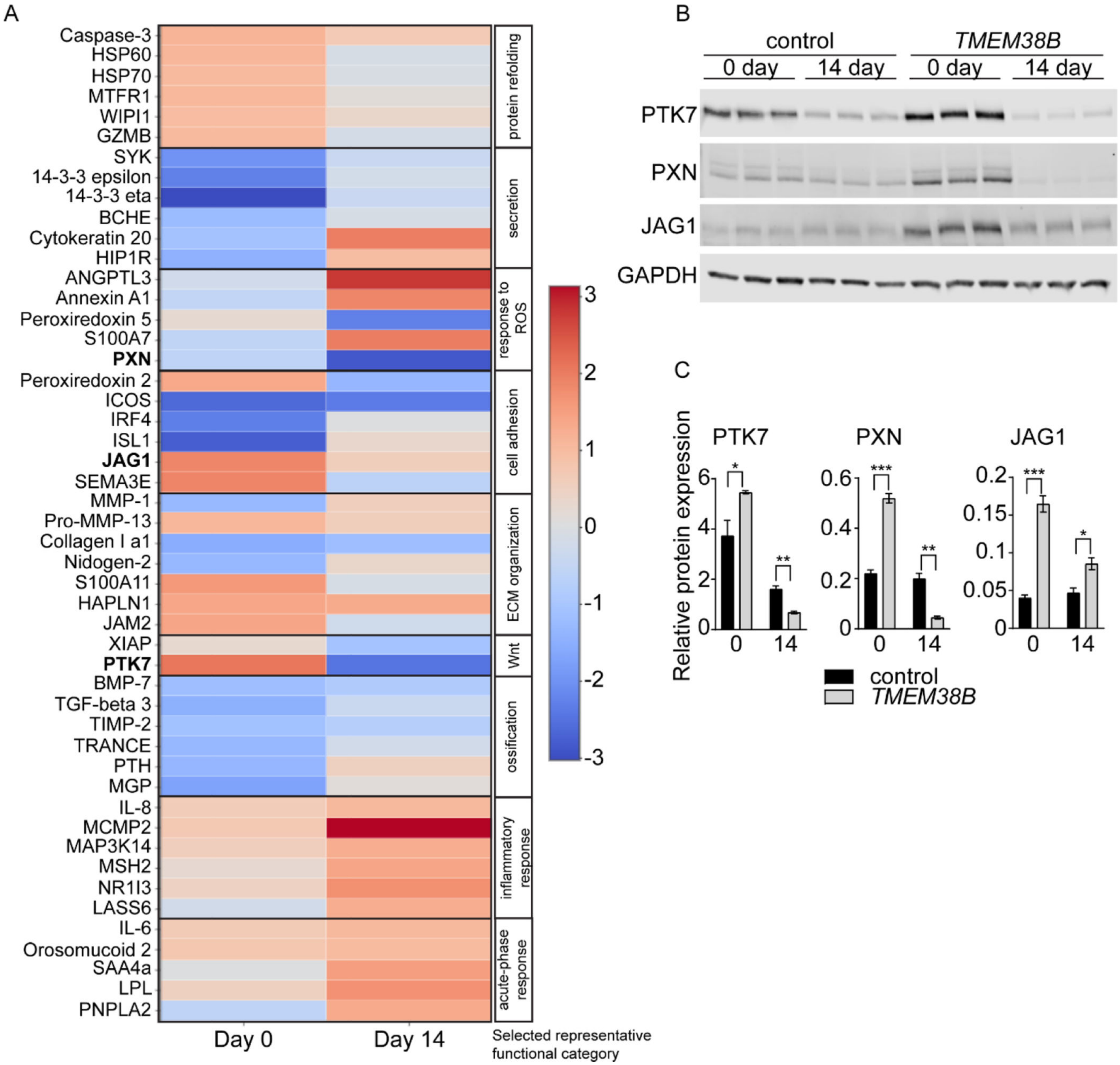

Figure 4.

Antibody array-based proteomics analysis in human *TMEM38B*-null osteoblasts. A. The heatmap of selected representative functional categories with selected subset of proteins. The colormap represents log2 fold change between *TMEM38B*-null osteoblasts and control. B. The top protein hits, PTK7, PXN, and JAG1 were validated by Western blot in control and human *TMEM38B*-null osteoblasts at Day 0 and 14. GAPDH was used as a loading control. C. Quantification of PTK7, PXN, and JAG1 protein levels normalized to GAPDH. Data are presented as means ± SEM. *P < 0.05, **P < 0.01, ***P < 0.001.

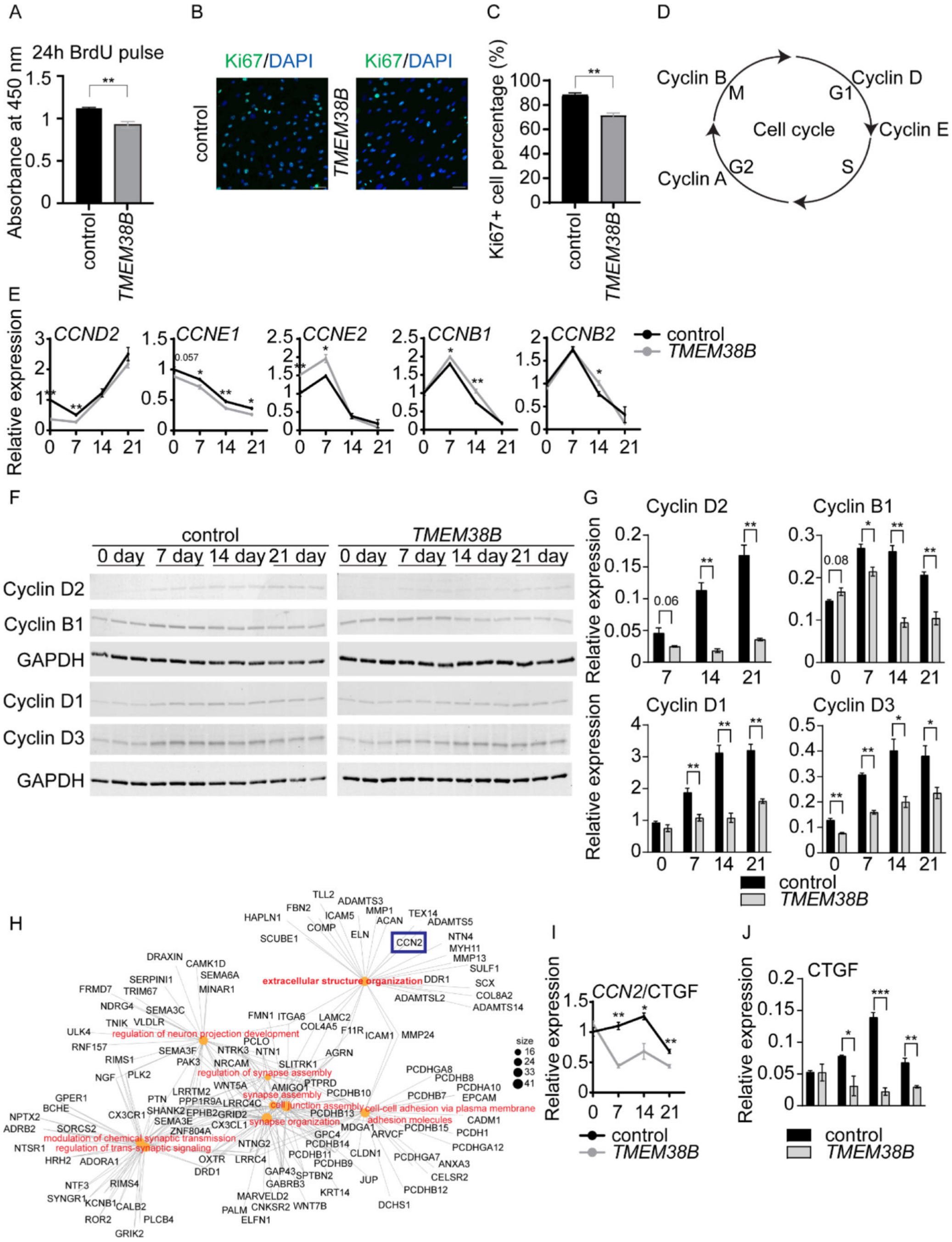

Figure 5.

Proliferation and cell cycle progression are disrupted in human *TMEM38B*-null osteoblasts. A. Cell proliferation graph of control and human *TMEM38B*-null osteoblasts treated with BrdU for 24h. Absorbance intensity was read at 450 nm. B. Immunocytochemistry of Ki67, proliferation marker, in control and human *TMEM38B*-null osteoblasts. DAPI was used as a counterstain. Scale bars, 50 μm. C. Double positive Ki67$^+$, DAPI$^+$ cells were normalized to total DAPI$^+$ cell number and expressed as a percentage. D. Diagram of cell cycle phases and specific cyclins involved in each phase. E. mRNA expression level of *CCND2*, *CCNE1*, *CCNE2*, *CCNB1*, *CCNB2* in control and human *TMEM38B*-null osteoblasts at Day 0, 7, 14 and 21 of differentiation. Expression was normalized to control mRNA expression at Day 0 of osteoblasts differentiation and evaluated by $^{\Delta\Delta}$Ct method. F. Western blots of cyclins (D2, B1, D1, and D3) in control and human *TMEM38B*-null osteoblasts at Day 0, 7, 14 and 21 of differentiation. GAPDH was used as a loading control. G. Quantification of cyclins (D2, B1, D1, and D3) protein levels normalized to GAPDH. H. RNA-Seq functional enrichment analysis presented by cnetplot of genes involved in downregulated pathways in human *TMEM38B*-null osteoblasts compared to control osteoblasts at Day 7, indicate *CCN2*/CTGF as a part of “extracellular structure organization” GO pathway. I. mRNA expression level of *CCN2*/CTGF in control and human *TMEM38B*-null osteoblasts at Day 0, 7, 14 and 21 of differentiation. J. Quantification of CTGF protein levels normalized to GAPDH. Data are presented as means ± SEM. $^*P < 0.05$, $^{**}P < 0.01$, $^{***}P < 0.001$.

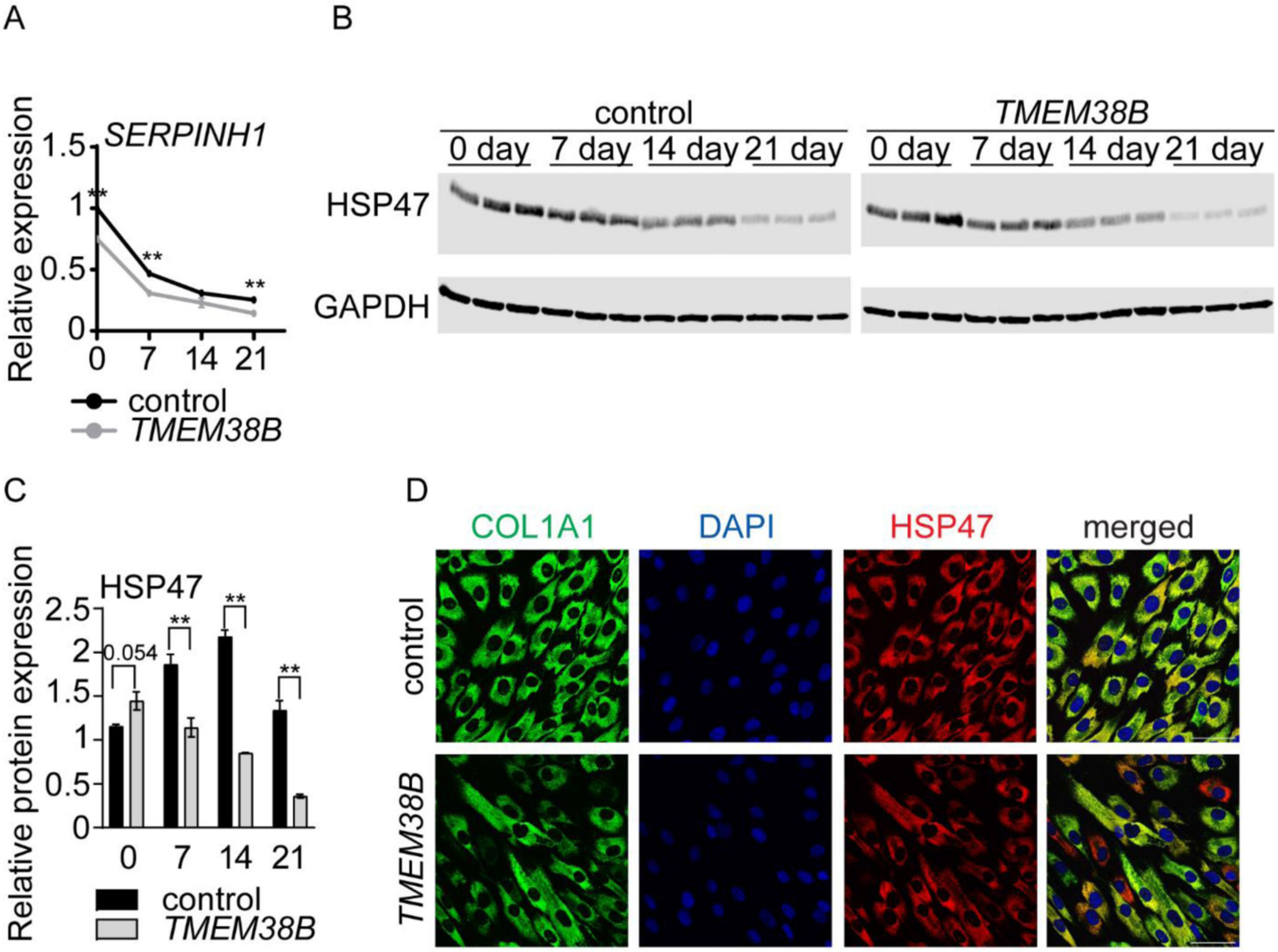

Figure 6.

Induced ER stress in human osteoblasts in absence of *TMEM38B*. A. mRNA expression level of *SERPINH1* in control and human *TMEM38B*-null osteoblasts at Day 0, 7, 14 and 21 of differentiation. Expression was normalized to control mRNA expression at Day 0 of osteoblasts differentiation and evaluated by $^{\Delta\Delta}$Ct method. B. Western blots of HSP47 protein, a marker of collagen ER retention, in control and human *TMEM38B*-null osteoblasts at Day 0, 7, 14 and 21 of differentiation. GAPDH was used as a loading control. C. Quantification of HSP47 protein levels normalized to GAPDH. D. Immunocytochemistry of COL1A1 and HSP47 proteins in control and human *TMEM38B*-null osteoblasts. DAPI was used as a counterstain. Scale bars, 50 μm. Data are presented as means ± SEM. $^{**}P < 0.01$.

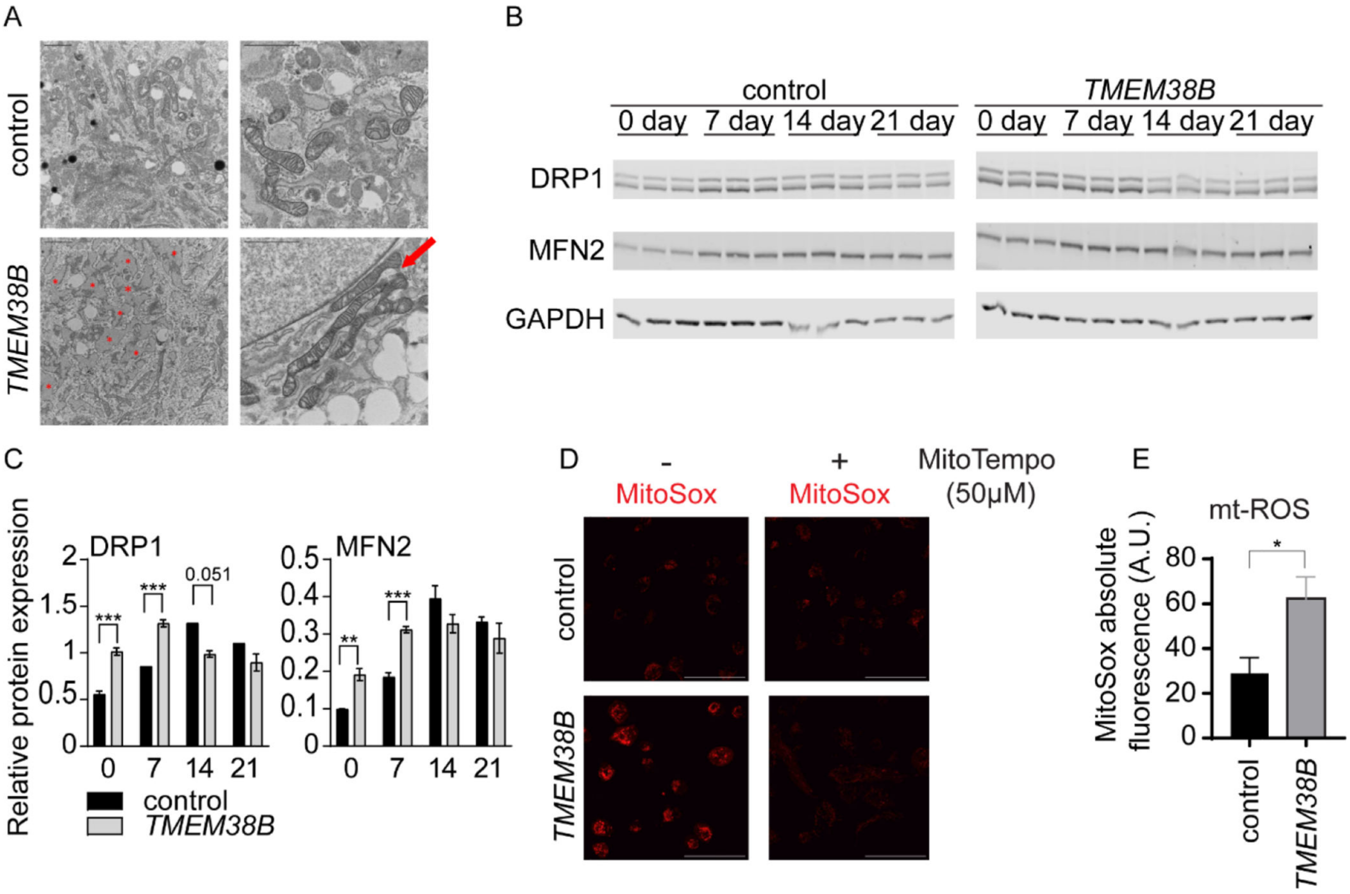

Figure 7.

Prolonged ER stress due to absence of *TMEM38B* causes alterations in mitochondrial function in human osteoblasts. A. Electron microscopy images of control and human *TMEM38B*-null osteoblasts. Red asterisks indicate dilated ERs, while red arrow points to elongated mitochondria. Scale bars, 2 µm. B. Western blots of DRP1 and MFN2 in control and human *TMEM38B*-null osteoblasts at Day 0, 7, 14 and 21 of differentiation. GAPDH was used as a loading control. C. Quantification of DRP1 and MFN2 protein levels normalized to GAPDH. D. Immunocytochemistry of MitoSOX Red, a specific dye for superoxide in mitochondria in live control and human *TMEM38B*-null osteoblasts. 50 µM of MitoTEMPO, a mitochondrial antioxidant and a superoxide scavenger, was applied to control and human *TMEM38B*-null osteoblasts for 24 h and stained with MitoSOX Red. Scale bars, 50 µm. E. Quantification of the mitochondrial ROS within the control and *TMEM38B*-null osteoblasts, by measuring the absorbance of MitoSOX Red fluorescence. Data are presented as means ± SEM. *P < 0.05, **P < 0.01, ***P < 0.001.

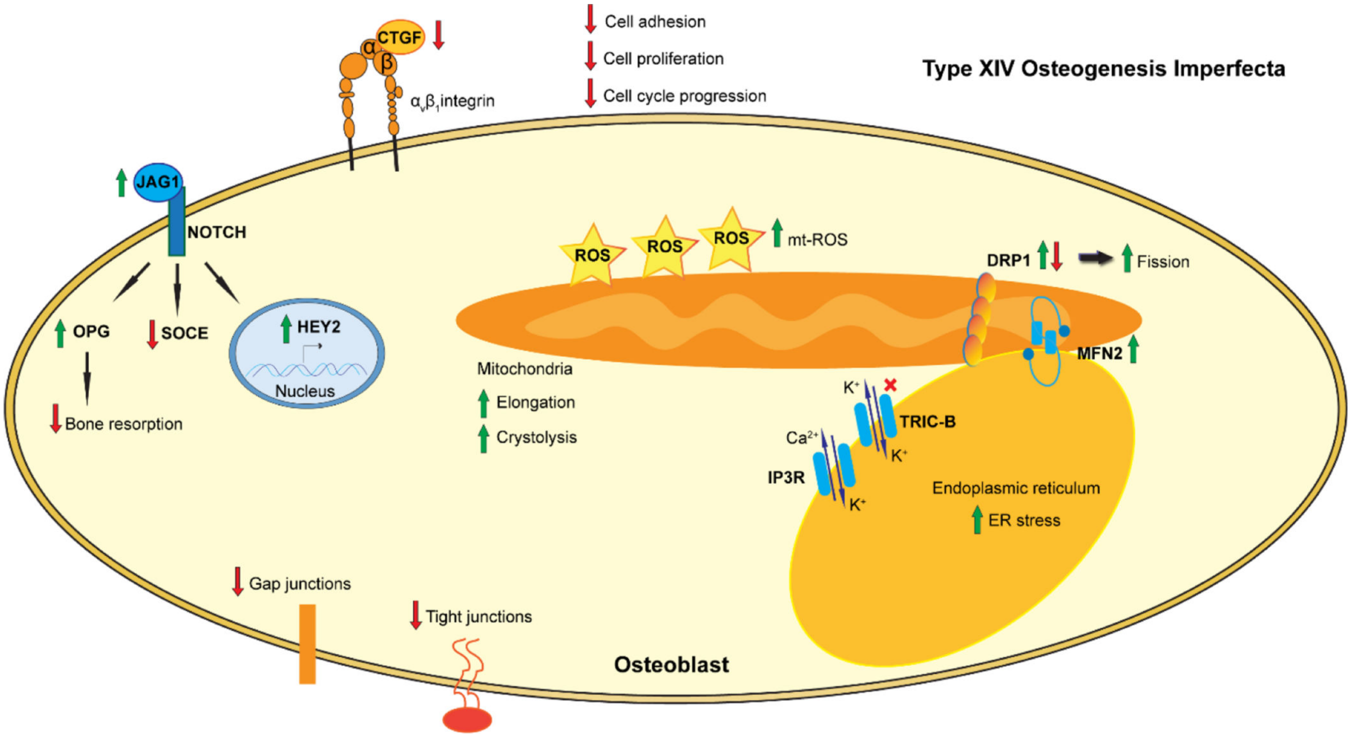

Figure 8.

Schematic of proposed underlying mechanisms of type XIV OI in osteoblasts. The TRIC-B channel, together with IP3R, regulates calcium flux from the ER to cytoplasm. Absence of TRIC-B in osteoblasts impairs release of ER calcium, further inducing ER stress. ER-mitochondria contact sites regulate calcium signaling, lipid trafficking and mitochondria fusion and fission processes. Prolonged ER stress due to TRIC-B deletion disrupts fusion/fission of mitochondria shown by altered fusion and fission markers MFN2 and DRP1 respectively, and mitochondria morphology. Further changes in calcium signaling increases ROS generation in mitochondria. Decreased cell adhesion slows down cell proliferation and cell cycle progression. Cell-cell communication is further affected by decreased gap and tight junctions. CTGF, which binds to $\alpha_V\beta_1$ integrin and enhances integrin-based cell adhesion of osteoblasts, is downregulated. Notch signaling is increased in absence of TRIC-B, shown by increased JAG1 protein and expression of downstream target gene *HEY2*. Increased Notch signaling further upregulates OPG, known to decrease bone resorption. In addition, Notch signaling affects store-operated calcium entry (SOCE), previously shown to be deficient in absence of TRIC-B channel.